CHALMERS
UNIVERSITY OF TECHNOLOGY

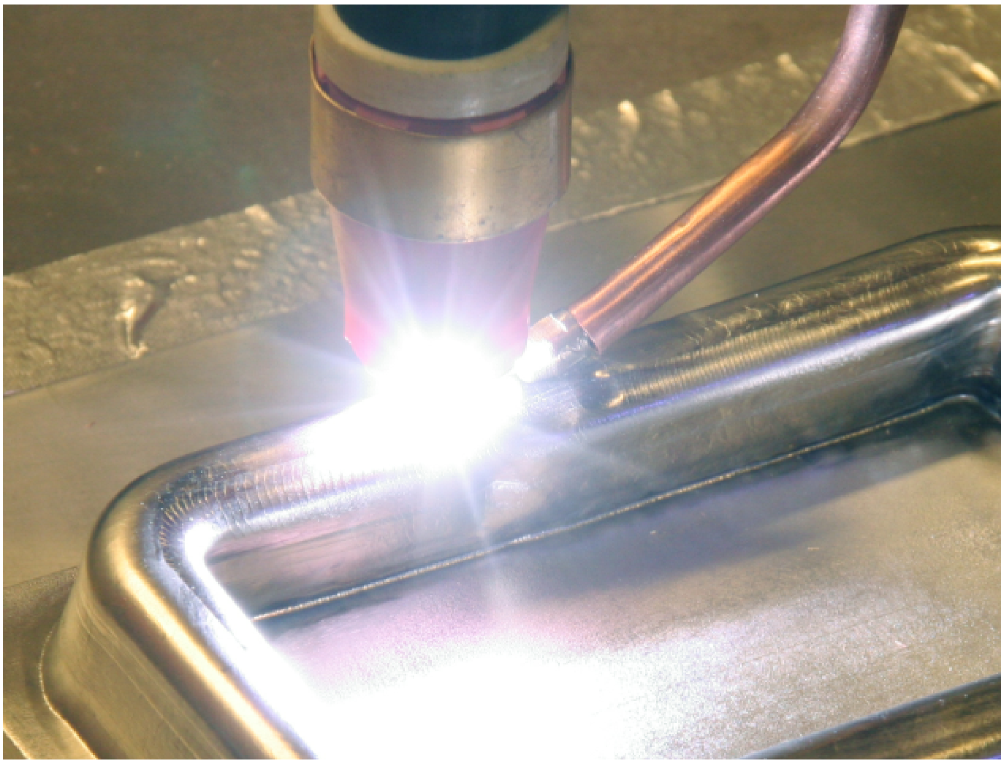

Modeling of Laser Metal Deposition

An Additive Manufacturing Method

Master's thesis in Sustainable Energy Systems

JOEL LARSSON

Department of Applied Mechanics
CHALMERS UNIVERSITY OF TECHNOLOGY
Gothenburg, Sweden 2016

Master's thesis 2016:24

Modeling of Laser Metal Deposition

An Additive Manufacturing Method

JOEL LARSSON

CHALMERS
UNIVERSITY OF TECHNOLOGY

Department of Applied Mechanics
Division of Material & Computational Mechanics
Chalmers University of Technology
Gothenburg, Sweden 2016

Modeling of Laser Metal Deposition
An Additive Manufacturing Method
JOEL LARSSON

Supervisor: Linda Larsson, GKN Aerospace.
Examiner: Magnus Ekh, Applied Mechanics.

Master's Thesis 2016:24
ISSN 1652-8557
Department of Applied Mechanics
Division of Material & Computational Mechanics
Chalmers University of Technology
SE-412 96 Gothenburg
Telephone +46 31 772 1000

Cover: Laser Metal Wire deposition by GKN Aerospace.

Typeset in LaTeX
Printed by [Chalmers Reproservice]
Gothenburg, Sweden 2016

Modeling of Laser Metal deposition
An Additive Manufacturing Method
JOEL LARSSON
Department of Applied Mechanics
Chalmers University of Technology

Abstract

The work presented in this thesis was carried out during the spring of 2016 at the Department of Applied Mechanics at Chalmers University of Technology in Göteborg, in close collaboration with GKN Aerospace in Trollhättan. The aim was to create a computational model inside the Matlab$^{®}$ environment that can be used to simulate temperature distributions in the substrate and the added material during Laser Metal-Wire Deposition (LMwD) of Ti-6Al-4V. Metal 3D-printing has opened up the possibility to go beyond the constraints of geometrical complexity, and enhance energy and manufacturing efficiency. Meanwhile, simulations have become a necessary tool to bridge the relation between process parameters and material properties. Simulations of temperature distributions can yield information that indicate the stability and accuracy of the process, e.g. melting depth, maximum temperature and microstructure.

The created model has been validated, and the results show satisfying consistency with experimental data. However, further analysis and comparisons are needed to better validate and increase the accuracy of the model.

Sensitivity analysis have been performed and Design of Experiments (DOE) involving the variation of the main process parameters (laser power, laser traverse speed and wire feed rate) has been executed. The results from the DOE have been analysed and a constituting process window for the main process parameters has been established.

Keywords: Additive Manufacturing, Laser Metal Wire Deposition, Modeling, Simulation, 3D-printing, Matlab.

Acknowledgements

Firstly, I would like to express my sincere gratitude to my supervisor, Dr. Linda Larsson at GKN Aerospace for her continuous support and contribution to the ongoing process of this Master's thesis. This work would not have been possible without her immense knowledge and guidance. Sincere gratitude are also directed towards my examiner, Prof. Magnus Ekh at Chalmers University of Technology for his feedback and monitoring. Furthermore, I want to thank Anders Sjunnesson, Almir Heralić, Kristina Domeij, Stefan Forsman, Hans Mårtensson and Eva Stenström at GKN Aerospace for their valuable input and feedback.

Joel Larsson, Göteborg, May 2016

Contents

Nomenclature

Abbreviations

AM	Additive Manufacturing
DOE	Design Of Experiments
LMD	Laser Metal Deposition
LMwD	Laser Metal-wire Deposition
LOF	Lack Of Fusion

Greek symbols

Variable	**Description**	**Unit**
α	Micro structure alpha phase	$-$
β	Micro structure beta phase	$-$
θ	Fluid coefficient of thermal expansion	$1/T$
μ	Dynamic viscosity	$kg/(ms)$
ν	Kinematic viscosity	m^2/s
ρ	Density	kg/m^3

Roman symbols

Variable	**Description**	**Unit**
A	Area	m^2
c	Specific heat	$J/(kgK)$
c_p	Specific heat under constant pressure	$J/(kgK)$
c_v	Specific heat under constant volume	$J/(kgK)$
d_w	Wire diameter	mm
D	Melt pool depth	mm
D_0	Length reference	mm
E	Total energy	J
E_1	Process trial one	$-$
E_2	Process trial two	$-$
H	Height	m
h	Convective heat transfer coefficient	$W/(m^2K)$
h_f	Latent heat of fusion	J/kg
h_v	Latent heat of vaporisation	J/kg
k	Thermal conductivity	$W/(mK)$
L	Significant length	m
L_l	Laser width	mm
L_w	Length of wire in laser	mm
m	Mass	kg
m_n	Mass per node	kg
n_l	Number of nodes under the laser	$-$
n_{fen}	Number of fully exposed nodes	$-$
n_{psn}	Number of partially shaded nodes	$-$
n_d	Number of nodes in width of string	$-$
P	Potential energy	J

P_l	Power input from laser	W
P_r	Power reflected	W
P_w	Power input to the wire	W
P_1	Power input to shaded nodes	W
P_2	Power input to fully exposed nodes	W
P_3	Power input to partially shaded nodes	W
p_t	Pause times	s
q	Heat flux	W/m^2
Q	Heat	J
Q_{inp}	Power input	W
Q_{dn}	Heat content newly deposited node	W
r	Reflectivity	$-$
S	Source term	W/m^3
s_l	Substrate length	mm
s_t	Substrate thickness	mm
s_w	Substrate width	mm
T_a	Ambient temperature	K
T_b	Boundary temperature	K
T_{bAl}	Aluminium boiling temperature	K
T_{bTi}	Titanium boiling temperature	K
T_{is}	Initial substrate temperature	K
Tc_1	Temperature thermocouple one	K
Tc_2	Temperature thermocouple two	K
Tc_3	Temperature thermocouple three	K
Tc_4	Temperature thermocouple four	K
T_{dn}	Temperature newly deposited node	K
T_f	Fluid bulk temperature	K
Tk_0	Zero critical temperature limit	K
Tk_1	First critical temperature limit	K
Tk_2	Second critical temperature limit	K
Tk_3	Second upper critical temperature	K
T_{m1}	Ti-6Al-4V melting start temperature	K
T_{m2}	Ti-6Al-4V melting end temperature	K
T_s	Surrounding temperature	K
t_t	Traverse time	s
t_s	Time step size	s
t_w	Time wire is exposed to laser	s
T_0	Temperature reference	K
U	Internal energy	J
v	Velocity magnitude	m/s
v_t	Traverse speed	m/s
v_w	Wire feed rate	m/s
W	Work	J

Dimensionless numbers

Variable	**Description**	**Definition**

Gr	Grashof number	$Gr = \frac{\theta g \rho^2 L^3 \Delta T}{\mu^2}$
Nu	Nusselt number	$Nu = \frac{hL}{k}$
Pr	Prandtl number	$Pr = \frac{\mu c}{k}$
Ra	Raylights number	$Re = Gr \cdot Pr$
Re	Reynolds number	$Re = \frac{vL}{\nu}$

List of Figures

List of Tables

1

Introduction

"Modeling of thermal distribution and thermal history in AM are crucial due to their significant effect on material property, microstructure, manufacturing deformation and defect occurrence" - Stefan Forsman, GKN Aerospace.

1.1 Background

Laser Metal deposition (LMD)[1] is a form of Additive Manufacturing (AM). AM itself, has evolved from processes involving rapid prototyping, where layer-upon-layer of a desired material can be added to construct complex geometries. The history of rapid prototyping goes back to the 1980s. Thus, the family of technologies evolved from this particular method, such as AM, are still in its youth. However, with the increasing development of these methods along with the development of computers, lasers and the introduction of effective and accurate modeling methods, the interest for AM as a manufacturing method to produce production parts, has grown rapidly [1].

GKN Aerospace Engine Systems has developed robotized Laser Metal-wire Deposition (LMwD), which is supposed to work as a complementary manufacturing method for low stressed areas in static jet engine components [2]. The current work focuses on the LMD process of the Ti-6Al-4V material. The developed AM technology involves using a metal wire as filler material, and the utilisation of a high power laser as a heat source. The laser beam melts the metal, creating string by string and layer upon layer of material [3].

Traditional manufacturing methods for aerospace components often generate high production costs and long lead times [4]. Today, the most common methods are forging and casting. In forging processes, more than half of the initial material often needs to be removed in order to create the desired shape. Therefore, forged components need to be largely oversized depending on the geometrical complexity of the final shape. This raises the production cost significantly when dealing with material such as nickel based super alloys and titanium. The limitations of casting comes mainly from the difficulties in creating complex geometries, while keeping the material integrity [5].

AM on the other hand, has opened up the possibility to go beyond the constraints of geometrical complexity, and it offers an alternative to high cost manufacturing processes. Its future potential for the industry as an established manufacturing method

---

[1] LMD: a general abbreviation that often refers to both metal-wire, and powder bed technology.

includes increased energy efficiency, and improved process yields [2].

Due to the relatively recent introduction of AM, the lack of experience and data contributes to a high degree of uncertainty concerning the quality of the end product. The relationship between material properties and process parameters is uncertain, and the different types of defects that can occur in AM process and how to detect them are yet to be investigated [1].

In order to use the method on a large scale in the aerospace industry, the AM process needs to be robust ensuring that strict safety and reliability requirements are met. Simulations of AM processes have become an important tool to evaluate the quality of the end product and its dependence on process parameters. Fast and accurate modeling programs can pin-point product malfunctions and help to establish reasonable process control. Inherent to the AM process is also large variation in thermal history, within builds and between builds, depending on a large number of process and geometric parameters. Investigating the effect of all parameters using traditional manufacturing trials would be very expensive and time consuming. Modeling of the thermal history therefore becomes a necessary tool to reduce the amount of manufacturing trials needed.

1.2 Objectives

At GKN Aerospace there is an ongoing process of further development of the LMD process, and several process trials have and will be performed. The main task of this thesis was to create a model for the simulation of temperature distributions during LMwD in Matlab®. This was done by improving and extending an existing simple thermodynamic model created by Dr. Linda Larsson at GKN Aerospace. In a later stage, the new model was to be validated and tuned against data from the process trials. The model includes heat transfer, process control and material properties. The expected result was to create an accurate and comparably fast thermodynamic model, and to establish a process window together with an increased understanding of the sensitivity to changes in different process parameters.

1.3 Constraints

The program do not include thermomechanical coupling of stress, strain, shape or deformation. The melt pool fluid physics is not modeled, and the examined process parameters are limited to a framework that concerns the process trials in general. The research is limited to the heat transfer and temperature distribution in the substrate and the added material. The post processing is constrained to the analysis of the results from the sensitivity analysis, and the design of experiments.

1.4 Research Questions

- Is the created Matlab® model computationally fast and accurate enough?
- How sensitive is the process to changes in different parameters such as initial wire temperature, ambient temperature and paus times?
- What span of values in the DOE for the concerning process parameters such as laser power, laser traverse speed and wire feed rates are safe to work within in order to not exceed critical temperatures?
- How does change in the main process parameters affect the depth of the melt pool, maximum temperature and temperature history?

2

Theory

2.1 Process description

In LMwD strings are generated by melting a metal wire that are constantly being fed into the eye of an high powered laser. The melted wire creates a melt pool on the substrate material before it forms a metallurgical bound with the substrate during solidification. By moving the process head and the wire feeder, a layer is formed.
The metal wire can be deposited in three ways, namely by *plunging*, *globular transfer* and *smooth transfer*. During plunging, insufficient melting causes the wire to plunge down into the melt pool where it melts. This can result in Lack of Fusion (LOF), where the fusion between the deposited material and the substrate is inadequate. On the contrary, globular transfer is a droplet-like transfer, where the surface tension no longer can bind the wire tip to the melt pool due to the wire reaching the melt temperature above the melt pool, which results in irregular string shapes. Smooth transfer gives the most accurate process but requires careful tuning of the parameters that govern the process in relation to desired deposition rate and the maximum heat input [4]. Figure 2.1 illustrates the formation of the beds on top of the substrate during smooth transfer.

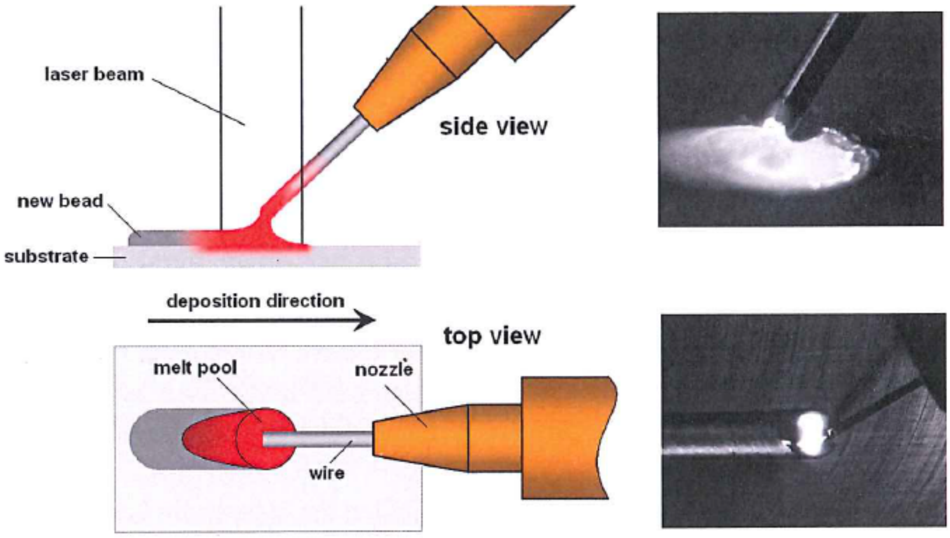

Fig. 2.1 *Left: Illustration of the laser-wire interaction. The molten metal solidifies into a bed by the relative motion of the welding tool and the substrate. Right: Top- and side view images of the real process [4]*

2.1.1 Process parameters

The main process parameters that control the process are the **laser power**, the **wire feed rate** and the **traverse speed**. These parameters control the energy input, the deposition rate, and both the width and height of the deposited layer. These parameters need to be tuned carefully in order to achieve a stable deposition. However, there are additional parameters worthy of being mentioned. For deposition of straight strings on flat surfaces, some important process parameters and their description are listed below [4].

Laser power: Controls the maximal energy input, and together with the size of the laser and the traverse speed, it also controls the melt pool size. Examples of different power distributions are top-hat and Gaussian distributions. Since the absorption is not equal for all wavelengths, the wavelengths of the laser also control the energy input [4].

Laser beam size and shape: Together with the laser power and the traverse speed, the laser beam size and shape govern the size and shape of the meltpool. Circular shapes are common but rectangular shapes can also be produced using diode lasers [4].

Wire feed rate: Controls the added mass per time unit, which consequently governs the height of the deposited layer, and the temperature of the deposited wire [4].

Wire diameter: An important parameter to take into consideration depending on laser beam size, since the wire shadows the substrate directly under itself. Logically, a larger wire requires more energy to be melt [4].

Wire angle: A higher angle decreases the sensitivity to deposition direction, but increases the sensitivity to wire feed rates [4].

Feeding direction: The direction of which the wire enters the melt pool can alter the process window of allowable wire feed rates. Examples of feed directions are front feeding, and back feeding. In front feeding the wire shades the nodes where no material has been deposited, and in back feeding the wire shades the nodes where material have been deposited [4].

Traverse speed: Controls the added mass per unit length, as well as the input energy per unit length. Low traverse speed results in high local energy input. However, a low speed makes the deposition process more easily controlled. For high traverse speeds, the path accuracy and motion system's acceleration most be carefully considered [4].

2.1.2 Deposition of several layers

So far, process parameters concerning single layer deposition onto a flat surface have been covered. However, the main purpose of additive manufacturing is to be able to print high quality 3D parts, which require additional layers to be deposited upon each other. In such cases, additional parameters need to be considered, such as deposition pattern, distance between strings and paus times between layers. The estimation of the layer height becomes extremely important in the process of achieving a continuous smooth deposition. The heat accumulation between the layers needs to be considered and the paus times between the deposited layers tuned accordingly [4]. The geometry after final layer deposition and heat accumulation due to short paus times is illustrated in Figure 2.2.

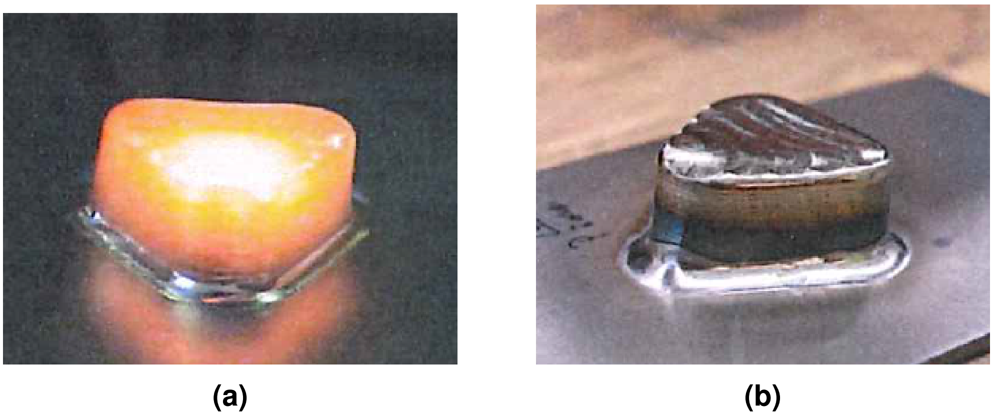

Fig. 2.2 *(a): Illustration of heat accumulation due to short paus times between layer depositions. (b): The geometry after final layer deposition (Heralić A., 2012)[4]*

2.2 Heat transfer

The following section gives a brief introduction to the energy conservation principle and the different modes of heat transfer, theory which forms an underlying basis to this Master's thesis.

2.2.1 First law of thermodynamics

The first law of thermodynamics states that the total energy for an isolated system is constant, i.e. energy cannot be created nor destroyed. This principle can be expressed as:

$$\Delta E = \sum Q_{out} - \sum Q_{in} + \sum W_{out} - \sum W_{in} \tag{2.1}$$

where ΔE is the net change of the total energy of the system, W is the mechanical work, and Q is the heat transfer. The total energy E is composed of three parts, namely, internal energy U, kinetic energy K and potential energy P. For a stationary system in vertical and horizontal direction, the changes in potential and kinetic energy are negligible, thus $\Delta E = \Delta U$.

In the absence of mechanical work, a differential form of the change in internal energy over time can be expressed as

$$\frac{dU}{dt} = \sum \dot{Q}_{out} - \sum \dot{Q}_{in} = m\, c(T)\, \frac{dT}{dt} \tag{2.2}$$

where c is the specific heat capacity, T is the temperature ans m is the mass of the system. Note, that for incompressible substances the constant-volume and the constant-pressure specific heats are identical, i.e. $c_p \approx c_v = c$ [6].

2.2.2 Conduction

Conduction is a diffusive transfer of energy. The heat flows from high energetic places to lower energetic places. In solids, this mode of energy transfer is a result of the energy transport by free-electrons in combination with vibrations of the lattice molecules. If the internal temperature distribution is known at given moment in time *Fourier's law*, Eq (2.3), can be used to find the heat flux in every point $\vec{x} \in \mathbf{R}^3$.

$$\vec{q} = -k\, \nabla T \tag{2.3}$$

where k is the conductivity, and ∇T is the temperature gradient. By conducting a general heat balance over the finite volume ($dV = dx\, dy\, dz$), see figure 2.3, and using the first law of thermodynamics, a partial differential equation can be derived. The solution to this equation yields the internal temperature of the control volume at a given time.

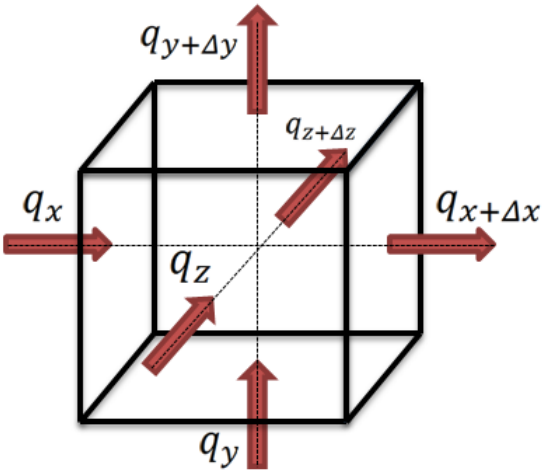

Fig. 2.3 *A finite element with volume $dV = dx\, dy\, dz$ and heat fluxes through its surfaces.*

Using the first law of thermodynamics, Eq (2.2), over the finite volume dV, and setting $\dot{Q}/A = q$ yields:

$$\rho c(T) \frac{\partial T}{\partial t} dV = -(q|_x - q|_{x+\Delta x}) dydz - (q|_y - q|_{y+\Delta y}) dxdz - (q|_z - q|_{z+\Delta z}) dxdy \tag{2.4}$$

Dividing by $dxdydz$ and taking the limit as Δx, Δy and $\Delta z \to 0$ yield:

$$\rho c(T)\frac{\partial T}{\partial t} = -\nabla \cdot \vec{q} \tag{2.5}$$

Inserting the expression for *Fourier's law* into Eq (2.5) yields:

$$\rho c(T)\frac{\partial T}{\partial t} = \nabla \cdot (k \nabla T) \tag{2.6}$$

Equation (2.6) is refered to as the *Fourier's partial differential equation*, and it must be satisfied for every point $\vec{x} \in \mathbf{R}^3$ for any moment in time [6][7].

2.2.3 Convection

The mode of convective heat transfer is divided into two mechanisms, namely, *natural convection* and *forced convection*. Convective heat transfer occurs when a fluid and adjoining surface exchange heat. In natural convection, the heat transfer causes density changes in the fluid near to the surface, this creates a buoyancy effect that displaces the heated fluid. This mechanism continues until the surface is in thermodynamic equilibrium with the surrounding fluid. If, on the other hand the fluid movement is not the primary cause of the heat transfer, but instead a result of interaction with an external source, it is called forced convection. The general rate equation for conduction can be expressed as:

$$q = h\Delta T \tag{2.7}$$

where h is the heat transfer coefficient, and ΔT is the temperature difference between the fluid and the solid boundary. The heat transfer coefficient is related to the mechanism of fluid flow, and the geometry of the heat releasing structure. It can be estimated by calculating the *Nusselts number* (Nu). In the case of natural convection, Nu is a function of the *Grashof number* (Gr) and the *Prandtl number* (Pr). In the case of forced convection, Nu is a function of the *Reynolds number* (Re) and Pr.

For horizontal plates Eq (2.8)-(2.9) can be used to calculate Nu [7]. A distinction is made whether the plate is facing up or down, as this clearly affects the induced buoyancy of the heated fluid. For a hot surface facing up:

$$\begin{aligned} Nu &= 0.54 Ra^{1/4} \qquad & 10^5 < Ra < 2 \cdot 10^7 \\ Nu &= 0.14 Ra^{1/3} \qquad & 2 \cdot 10^7 < Ra < 3 \cdot 10^{10} \end{aligned} \tag{2.8}$$

and for a hot surface facing down:

$$Nu = 0.27 Ra_L^{1/4} \qquad 3 \cdot 10^5 < Ra < 10^{10} \tag{2.9}$$

here Ra is referred to as the dimensionless *Raylights number*, which is a product of Gr and Pr.

2.2.4 Radiation

Unlike convection and conduction, radiation does not need a medium to traverse in. In fact, the presence of a medium will impede the radiation between two surfaces rather than to enhance it. The energy released from a body, at all wavelengths and in all directions per unit area, is called the total emissive power E. The ratio between the total emissive power and the total emissive power for a black body E_b is called the emissivity ϵ, Eq (2.10).

$$\epsilon = \frac{E}{E_b} \tag{2.10}$$

Integrating Planck's law of radiation from zero to infinity yields the Stefan-Boltzmann relation, which describes the total emissive power for a black body as a function of temperature

$$E_b = \sigma T^4 \tag{2.11}$$

where $\sigma = 5.670367 \cdot 10^{-8}\ Wm^{-2}K^{-4}$ is the Stefan-Boltmann constant, and T is the temperature of the black body. If a non ideal black body is radiating energy to a cooler surrounding of temperature T_s [7]. The total emissive power released per unit area can be calculated as:

$$E = \epsilon\sigma(T^4 - T_s^4) \tag{2.12}$$

2.3 Introduction to Ti-6Al-4V

The titanium alloy, Ti-6Al-4V (Ti64), is a two phase alloy containing 6wt% aluminium and 4wt% vanadium. It is the most commonly used titanium alloy today, and the aerospace industry accounts for over 80% of its total usage. Within the aerospace industry, the material is extensively used for engine components and airframe structures. The material has also been proven useful in surgical implants and various application areas can also be found in marine and automotive industry [8]. The attractiveness lies mainly in its high strength, toughness and corrosion resistance, as well as its good tensile and fatigue strength [9][3].
Ti64 exists in numerous chemical compositions, an example in Table 2.1. Higher concentration of particularly oxygen and nitrogen yield a higher strength of the material. Conversely, lower concentration of oxygen, nitrogen and aluminium will increase the ductility [8].

Table 2.1: Typical chemical composition of Ti-6Al-4V alloys

Element	Al	C	Fe	H	N	O	V	Ti
Composition (wt%)	6	0.1	0.4	0.015	0.05	0.2	3.4-4.5	balance

2.3.1 Phase transitions

Titanium alloys can be divided into three main groups, namely, alpha alloys (α), beta alloys (β) and alpha-beta alloys ($\alpha - \beta$). The α-phase is characterized by its *hcp* structure, and the beta phase by its *bcc* structure. Pure titanium undergoes a change in microstructure from an α- to β-phase when the temperature is raised through 1156 K [8]. For alloys, such as Ti64 the α- and β-phases are separated by a two phase region, ($\alpha - \beta$). The transition from this phase to the β-phase occurs around 1220 K [10]. Aluminium and oxygen are known to be α stabilizers, thus, they increase the transition temperature of the α-phase, while elements such as vanadium are β stabilizers. ($\alpha - \beta$) alloys such as Ti64 generally possess good fabricability, high room temperature strength and moderate elevated temperature strength [8].

2.4 Thermal properties of Ti-6Al-4V

Information crucial to the accuracy of the model, such as material parameters and temperature dependent thermodynamic properties of Ti64, are listed in the sections below.

2.4.1 Constants

In table 2.2, latent heat of fusion h_f, latent heat of vaporization h_v, temperature when the material starts to melt T_{m1}, temperature when the material is completely melted T_{m2}, the boiling temperature of aluminium T_{bAl}, and the boiling temperature of titanium T_{bTi} are listed. These constants are implemented in the model to account for phase transitions of Ti64.

Table 2.2: Thermodynamic properties of Ti64 used in the simulations. (ASM Aerospace Specification Metals Inc, 12 April 2016) [11]

Parameter	Value	Unit
h_f	360000	J/kg
h_v	8878768	J/kg
T_{m1}	1877	K
T_{m2}	1933	K
T_{bAl}	2743	K
T_{bTi}	3560	K

2.4.2 Thermal capacity

A temperature dependence for the specific heat capacity c has been proposed by Boyer [8] in the interval of $0 < T < 400$ K, by Boivineau [10] in the interval of $400 < T < 1400$ K, and by Cezairliyan [12] in the interval of $1400 < T < T_{m2}$ K. The liquid specific heat is assumed constant [11]. These dependencies can be observed in Figure 2.4, The vertical lines represent the $(\alpha - \beta)$ phase to the β phase transition, the melting temperature of Ti64, the aluminium boiling temperature, and the titanium boiling temperature. The specific heat capacity reaches its maximum in the $(\alpha - \beta)$ phase, and rapidly decreases to its minimum in the $(\alpha - \beta)$-β transition.

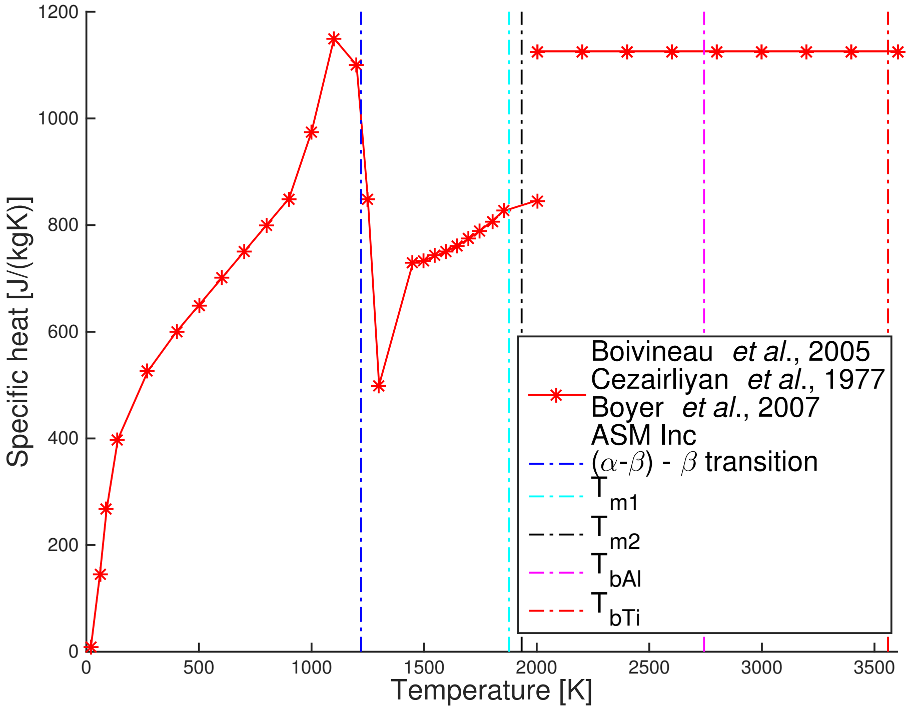

Fig. 2.4 *Specific heat capacity of Ti-6Al-4V vs temperature in the interval* $0 < T < T_{bTi}$ K.

Figure 2.5 illustrates the heat per unit mass Q/m as a function of temperature for Ti64. This curve is calculated using Eq. (2.13), together with the information presented in Table 2.2, and Figure 2.4. The heat of vaporisation is approximately 25 times larger than the latent heat of fusion. The results in Figure 2.5 are used to find the temperature of each internal node when the energy content of the node is known.

$$\begin{aligned}
Q(T) &= \int_{T_{ref}}^{T} m\,c(T)dT && T_{ref} < T < T_{m1} \\
Q(T) &= \int_{T_{ref}}^{T} m\,c(T)dT + m\,h_f && T_{m1} < T < T_{m2} \\
Q(T) &= \int_{T_{ref}}^{T_{m2}} m\,c(T)dT + \int_{T_{m2}}^{T} m\,c_l dT + m\,h_f && T_{m2} < T < T_{bTi}
\end{aligned} \tag{2.13}$$

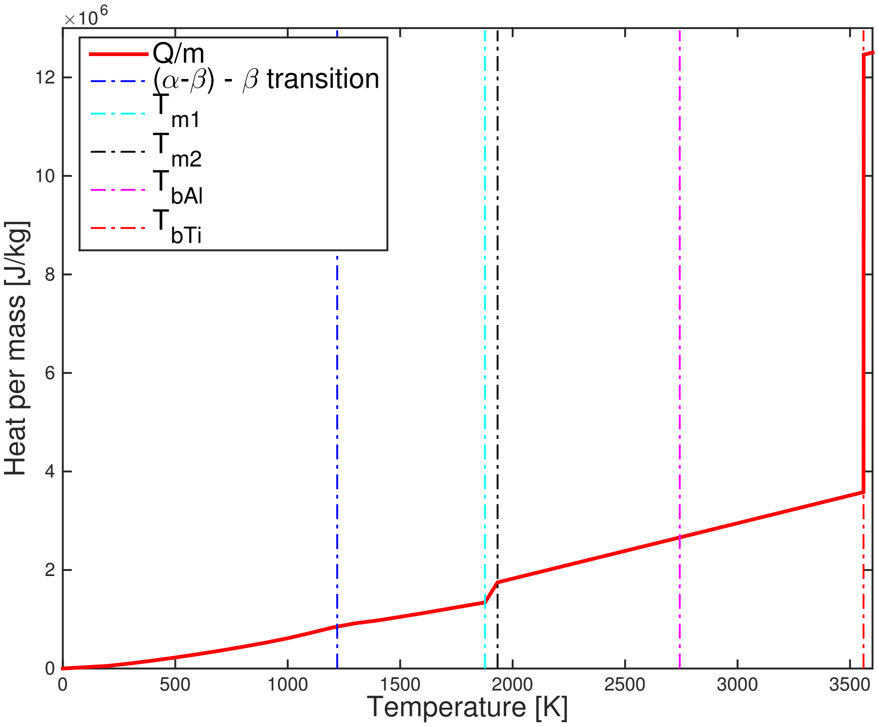

Fig. 2.5 *Heat per unit mass vs temperature in the interval* $0 < T < T_{bTi}$ K.

2.4.3 Conductivity

Figure 2.6 shows the conductivity of Ti64 in the temperature interval $200 < T < T_{m2}$ K. The conductivity increases linearly with temperature and is assumed to be unaffected by phase changes within the interval. Temperature dependence in the interval $200 < T < 1400$ K is proposed by Veiga [13]. Dependencies in the β-phase interval, $1400 < T < 1933$ K, and in pure liquid phase $T > 1933$ K, have been proposed by Boivineau [10].

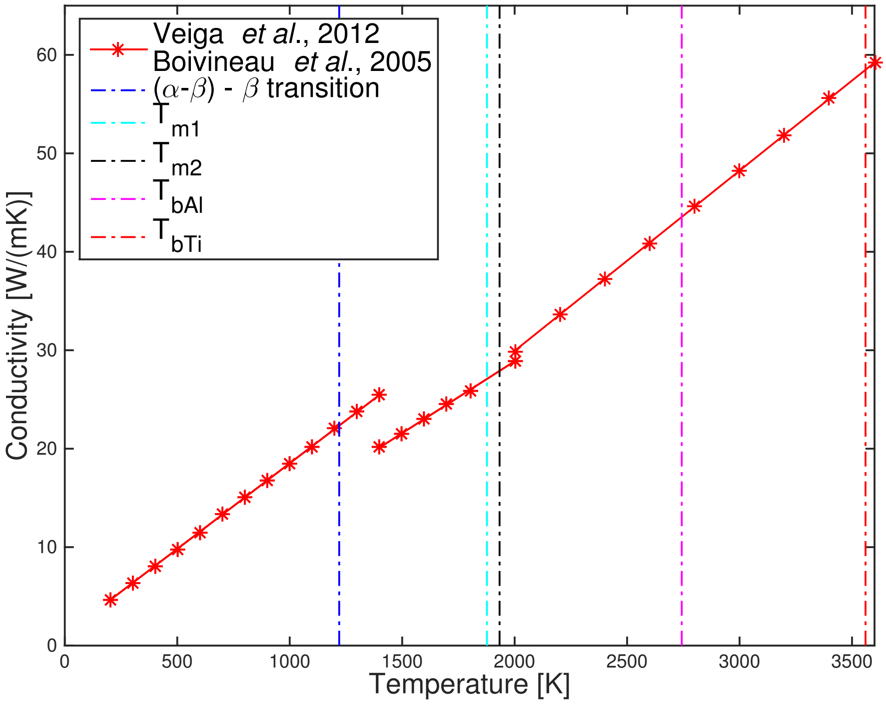

Fig. 2.6 *Conductivity of Ti-6Al-4V vs temperature in the interval* $200 < T < T_{bTi}$ K.

2.4.4 Emissivity

Temperature dependence for the emissivity of Ti64 has been proposed by Labudovic [14] in the temperature interval of $200 < T < 1600\ K$, and by Boivineau [10] in the temperature interval of $1788 < T < 1933\ K$, and in the liquid phase, see Figure 2.7.

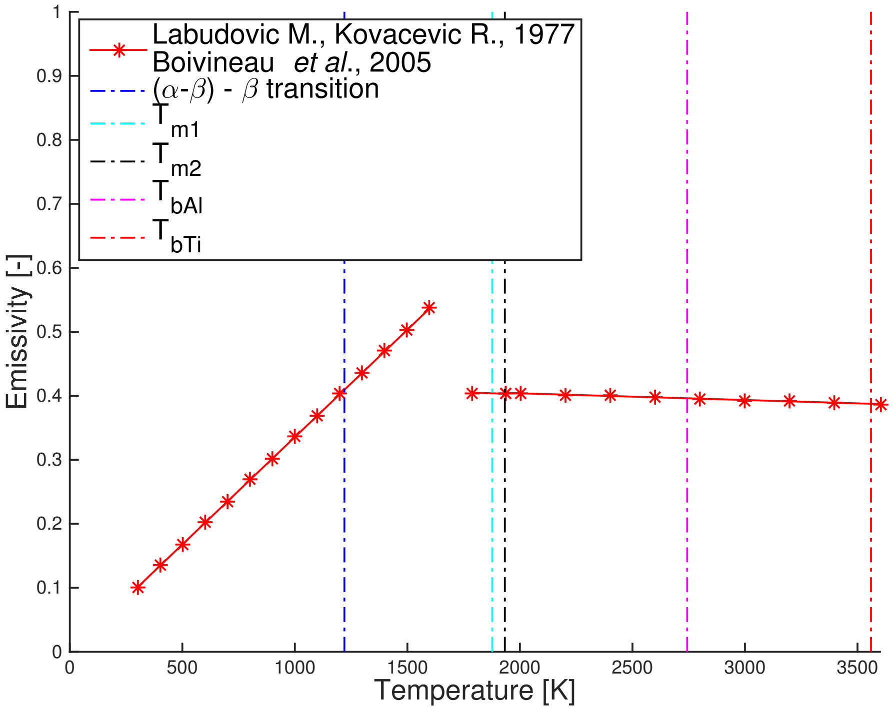

Fig. 2.7 *Emissivity of Ti-6Al-4V vs temperature in the interval* $200 < T < 1800\ K$*. The vertical lines represent the* $(\alpha - \beta)$ *phase to the* β *phase transition, temperature when Ti64 starts to melt* T_{m1}*, temperature when Ti64 is completely melted* T_{m2}*, aluminium boiling temperature* T_{bAl}*, and the titanium boiling temperature* T_{bTi}*.*

2.5 Finite volume method

In the finite volume method, the integral form of the conservation equations are used as a starting point. By integrating the heat equation, Eq (2.6) with the addition of a source term S, over a control volume, the integral form can be found:

$$\int_V \rho c(T) \frac{\partial T}{\partial t}\, dV = \int_V \nabla \cdot (k \nabla T)\, dV + \int_V S\, dV \tag{2.14}$$

The principle of this method is local conservation. In order to obtain a numerical solution to Eq (2.14), the domain needs to be discretized. In the finite volume method, the domain is divided into a finite number of sub-volumes, see Figure 2.8. The grid lines defines the boundaries of the control volumes, and the computational nodes where the values are stored, are for a structured grid located in the middle of the cell volume.

Each node can be identified by a set of indices, (j, i) in 2D. These indices represent the coordinates of the nodal values. The solution of the conservation equation (2.14) is approximated by the solution of a system of algebraic equations, in which the node values constitute the unknowns [15].

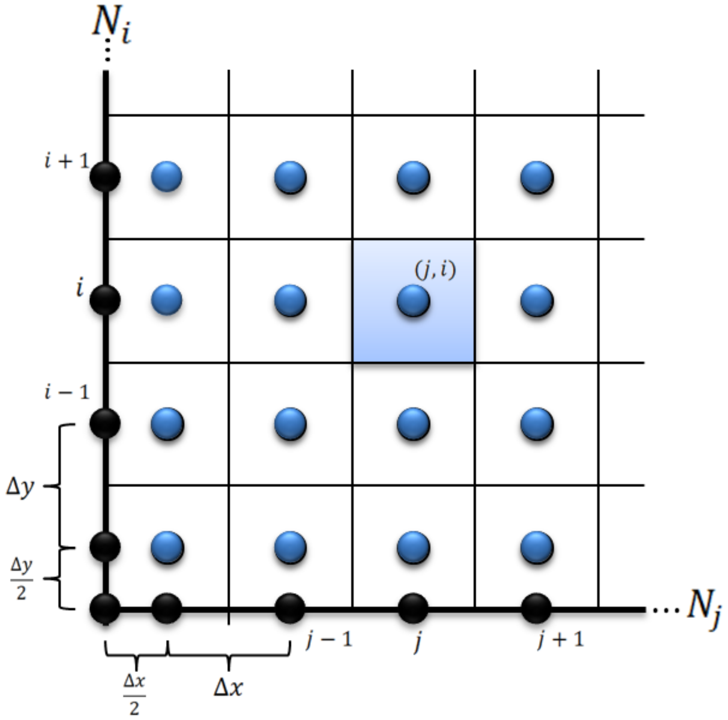

Fig. 2.8 *Example of a 2D structured Cartesian grid for finite volume methods, each black nodes constitutes boundary nodes, and blue nodes are internal nodes.*

2.5.1 Central differencing

The face values of the derivatives can be approximated with central differences as:

$$\left(\frac{\partial \phi}{\partial x}\right)_{x_j} = \lim_{\Delta x \to 0} \frac{\phi(x_j + \Delta x/2) - \phi(x_j - \Delta x/2)}{\Delta x} \approx \frac{\phi_{j+1/2} - \phi_{j-1/2}}{x_{j+1/2} - x_{j-1/2}} \tag{2.15}$$

This approximation is second order accurate assuming an equidistant grid, which can be shown by studying the accuracy of the following expression:

$$\frac{1}{\Delta x}\int_w^e \frac{d^2\phi}{dx^2}dx = \frac{1}{\Delta x}\left[\left.\frac{d\phi}{dx}\right|_e - \left.\frac{d\phi}{dx}\right|_w\right] = \frac{1}{\Delta x^2}\left[\phi_E - 2\phi_P + \phi_W\right] \tag{2.16}$$

Here the face values are $(d\phi/dx)_e = (\phi_E - \phi_P)/\Delta x$ and $(d\phi/dx)_w = (\phi_P - \phi_W)/\Delta x$. For simplicity $x_{j-1/2} = w$, $x_{j+1/2} = e$, and $x_j = P$, representing the west, east and middle point values respectively, see Figure 2.9.

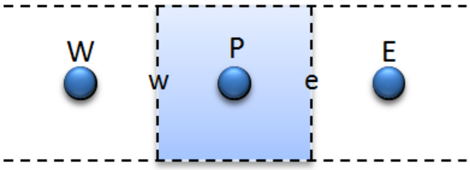

Fig. 2.9 *Illustration of a 1D set up of nodes, middle node denoted with capital P, east node E and the West node W, west border of control volume denoted with lower case letter w, and east boundary e.*

Taylor expanding ϕ_E and ϕ_W around ϕ_P yield:

$$\phi_E = \phi_P + \Delta x\left.\frac{d\phi}{dx}\right|_p + \frac{\Delta x^2}{2!}\left.\frac{d^2\phi}{dx^2}\right|_p + \frac{\Delta x^3}{3!}\left.\frac{d^3\phi}{dx^3}\right|_p + \mathcal{O}(\Delta x^4) \tag{2.17}$$

$$\phi_W = \phi_P - \Delta x\left.\frac{d\phi}{dx}\right|_p + \frac{\Delta x^2}{2!}\left.\frac{d^2\phi}{dx^2}\right|_p - \frac{\Delta x^3}{3!}\left.\frac{d^3\phi}{dx^3}\right|_p + \mathcal{O}(\Delta x^4) \tag{2.18}$$

Adding Eq (2.17) and Eq (2.18) into Eq (2.16) yield:

$$\frac{1}{\Delta x}\int_w^e \frac{d^2\phi}{dx^2}dx = \left.\frac{d^2\phi}{dx^2}\right|_p + \Delta x^2\left.\frac{d^4\phi}{dx^4}\right|_p + .. = \left.\frac{d^2\phi}{dx^2}\right|_p + \mathcal{O}(\Delta x^2) \tag{2.19}$$

Thus, the expression in Eq (2.19) is second order accurate.

2.5.2 Time Stepping

The approach of solving transient problems can be divided into *explicit* and *implicit* methods. The fully explicit scheme is only first order accurate, and requires no iterations compared to the fully implicit scheme, which is unconditionally stable. For explicit time stepping the following criteria need to be fulfilled in order to ensure convergence:

$$\Delta t = \frac{\rho c \Delta x^2}{2k} \tag{2.20}$$

where Δx is the grid spacing, ρ the density, k the conductivity and c the specific heat capacity. This is a severe restriction that only allows for very small time steps. However, it comes with the advantage of being computationally cheap since iterations are not needed in each time step [16].

2.5.3 Boundary conditions

To quantify the thermal interaction of the substrate and deposited strings with the surrounding fluid, an energy balance is conducted over the boundary node, where the emissive power Eq (2.12), and the convective heat transfer Eq (2.7), are equal to Eq (2.3). Since the boundary is two dimensional, no energy can be stored, and the balance yields:

$$-k\nabla T \cdot \vec{n} = \epsilon\,\sigma(T_b^4 - T_f^4) + h(T_b - T_f) \tag{2.21}$$

where $\vec{n}$ is the normal vector to the boundary, T_b is the temperature of the boundary node, and T_f is the temperature of the fluid. Introducing the radiative heat transfer coefficient h_{rad}, described by Eq (2.22):

$$h_{rad} = \epsilon\sigma(T_b^2 + T_f^2)(T_b + T_f) \tag{2.22}$$

Eq (2.21) simplifies to:

$$-k\nabla T \cdot \vec{n} = (h_{rad} + h)(T_b - T_f) \tag{2.23}$$

For the boundary node between two solids with internal node temperatures closest to the boundary of T_1 and T_2, and with conductivity k_1 and k_2 respectively, the energy balance takes the form of Eq (2.24).

$$k_1\nabla T_1 \cdot \vec{n_1} = -k_2\nabla T_2 \cdot \vec{n_2} \tag{2.24}$$

[17]

3

Methods

3.1 Approach

An initial model programmed in Matlab® for simulation of temperature distribution was created by Dr. Linda Larsson at GKN Aerospace in Trollhättan. This model has served as a fundamental building block on which improvements and extensions have been added to accurately describe the ongoing process trials at GKN. By the help of data from different process trials, the model could be tuned.
A sensitivity analysis has been performed on different parameters involved in the simulation in order to achieve a better understanding of their influence. A DOE has also been established and the constituting process windows examined. The approach of this thesis work is summarised below.

- Literature studies
- Existing model learning & testing
- Model improvement & extension
- Model tuning to fit data from process trials
- Sensitivity analysis
- DOE
- Compile information & analyse results

3.2 Model tuning

Data from four different thermocouples (Tc_1, Tc_2, Tc_3 and Tc_4) from two different process trials (E_1 and E_2), each with different setups, has been used as reference when tuning the model. The simulation settings, i.e. the process parameters, geometry and initial temperatures, were set in accordance with the settings used in E_1 and E_2. By using the results from the sensitivity analysis, the accuracy of the model could be maximised.

3.2.1 Process trial $\mathbf{E_1}$

Figure 3.1 illustrates the geometrical setup of process trial E_1 and the placing of the thermocouples. The thermocouples are placed on the bottom of the substrate. Five strings were deposited side by side, in five layers, thus, each layer consisted of five strings. Pause times were applied between each deposited string, during which the laser was shut off. The pause times were approximately equal for all 25 strings.

The direction of deposition was in positive x-direction, and each new string started at the top of the last deposited string in positive y-direction. In Figure 3.1, each string is numbered in the order of its deposition.

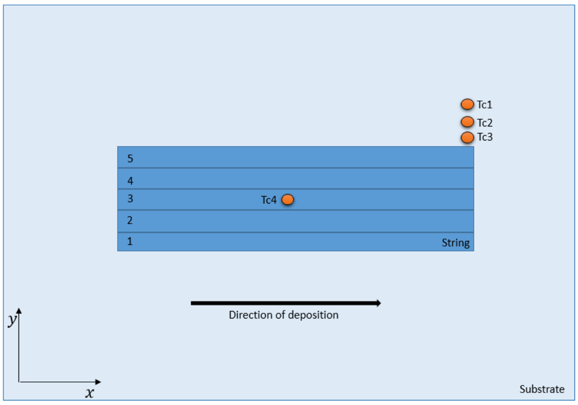

Fig. 3.1 *yx-view of geometrical dimensions and placings of the thermocouples* Tc_1, Tc_2, Tc_3 *and* Tc_4 *of process trial* E_1.

3.2.2 Process trial E$_2$

Figure 3.2 illustrates the geometrical setup of process trial E_2 and the placing of the thermocouples. The thermocouples were placed on the bottom of the substrate. Three strings were deposited with gaps between them, and the thermocouples were placed symmetrically between the strings. The pause time between the second and the third string was approximately 35 times longer than the pause time between the first and the second string.

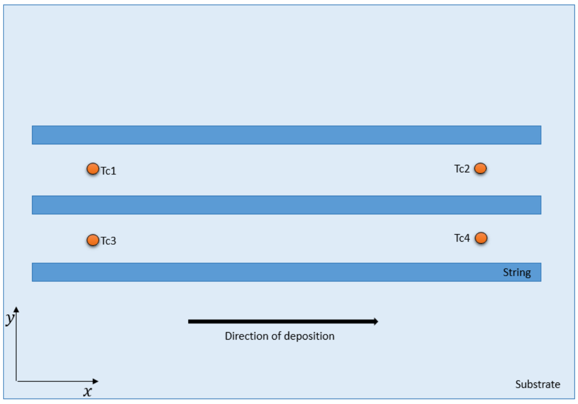

Fig. 3.2 *yx-view of geometrical dimensions and placings of the thermocouples* Tc_1, Tc_2, Tc_3 *and* Tc_4 *of process trial* E_2.

3.3 Sensitivity analysis

A sensitivity analysis was performed in order to achieve an understanding of the sensitivity to changes in specific thermodynamic parameters, substrate height, grid resolution and time stepping. This was done by simply varying the values of the parameters, and observe the deviations between the results. The temperature in the positions of the thermocouples Tc_1 and Tc_4, as well as the maximum temperature in the domain T_{max}, was studied in a 100 second interval. The process parameters and geometry were set to those used in E_1.

3.4 Design of experiments

A DOE was established to study the variation of process parameters under certain conditions. Similar process trials will be conducted at GKN Aerospace, and the DOE is suppose to work as a frame of reference for those trials. Laser power, traverse speed and wire feed rate were varied, as well as pause times between the deposited strings. Pause times of 50 % and 75 % of the nominal value were used, and laser powers, traverse speeds and wire feed rates of 120 % and 80 % of the nominal values were used. Figure 3.3 shows the geometrical setup for the DOE. Three strings, side by side, in three layers are deposited.

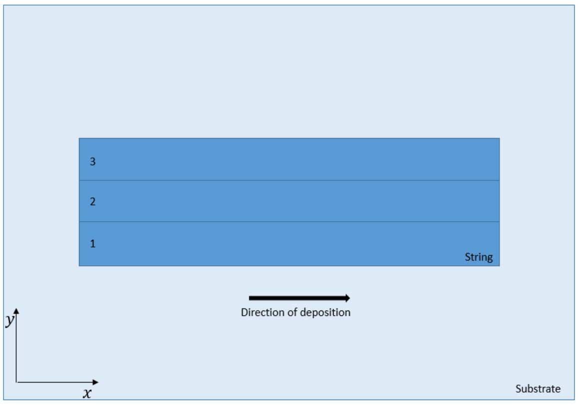

Fig. 3.3 *yx-view of the setup for the DOE.*

3.5 Simulation model

This section summarises the assumptions, the general algorithm, discretization of the heat equation and the implementation of the boundary conditions. Information necessary for the reader to form an understanding of the created model.

In order to accurately describe the ongoing process trials the model needed to include pause times, several strings side by side, layers upon layers, and also the possibility to alter the process parameters and geometry. The different input parameters are summarised in Table 3.1. The output gives the temperature in each node, from which post processing can give melting depth, micro structure profile and stability of the process.

Table 3.1: Specific input parameters (process parameters, constants and temperatures).

Process parameters	**Constants**	**Temperatures**
Laser power	Percent reflection	Ambient temperature
Traverse speed	Wire diameter	Wire temperature
Wire feed rate	Wire length in laser	Substrate temperature
Pause times	Heat transfer coefficient	
Traverse time	Laser width	
# strings	Substrate height	
# strings/layer	Substrate length	
# layers	Substrate width	
Front/back feeding		

3.5.1 Assumptions

The assumptions used to simplify the problem are listed below.

- The laser power is top hat distributed, and the geometry of the laser is square.
- The surrounding fluid is air, and the temperature inside the working environment remains constant throughout the simulations.
- The substrate is not mounted, thus it is completely surrounded by the fluid.
- The wire temperature remains constant throughout the simulations.
- The metal deposition occurs directly from wire to substrate, and no fluid calculations are accounted for.
- The width of the deposited bead are set in advantage. Thus, the spreading of the bed is limited to the change in height, which is controlled by the traverse speed and the wire feed rate.
- The heat transfer coefficient is constant throughout the domain.

3.5.2 Discretization of the domain

The domain can be divided into two regions, namely, the substrate (*lower domain*), and the above layers (*top domain*). The grid spacing within the lower domain is equidistant, and in order to fill the substrate with equally volumed cells (Δx^3), the distance from the boundary nodes to their closest neighbours are half of the internal grid spacing, see Figure 2.8. The layer height of the top domain is controlled by the traverse speed and the wire feed rate, (section 2.1.1), and Eq (3.1) gives the deposited height:

$$h_{bed} = \frac{\pi}{4} \frac{d_w^2 \, v_w}{\Delta x \, v_t \, n_d} \tag{3.1}$$

where v_w is the wire feed rate, Δx is the width of the element, v_t is the traverse speed, n_w is the number of nodes in the width of the deposited string, and d_w is the wire diameter. The cell height in the top domain is set to the layer height. Thus, the cell volumes in the top domain are equal to $h_{bed} \cdot \Delta x^2/2$.

3.5.3 Temperature of newly deposited nodes

The heat content of the newly deposited node is calculated with Eq 3.2.

$$Q_{dn} = Q_w + \frac{\pi}{4} \frac{d_w^2 \, L_w \, \rho}{m_n} \, P_w \, t_w \tag{3.2}$$

where Q_w is the heat content of the initial wire, P_w is the power absorbed by the wire, L_w is the length of the wire that shadows the laser, m_n is the mass per node in the deposited layer, and t_w is the time the wire is exposed to the laser. Thus, Q_{dn} is dependent upon the traverse speed and the wire feed rate, since, $t_w = f(v_w)$, and $m_n = f(v_t)$. With the information shown in Figure 2.5, Q_{dn} is used to find the temperature of the newly deposited node.

3.5.4 Discretization of the heat equation

Figure 3.4 illustrates a cell volume and its adjacent nodes. T_{n^+} and T_{n^-} denotes the face values at the cell boundaries in negative and positive n-directions, $T_{n^{++}}$ and $T_{n^{--}}$ denote the adjacent nodal values in the neighbouring cells. In order to find the value of T inside the cell boundaries, the heat equation needs to be transfered from a continuous differential equation to an algebraic discrete equation.

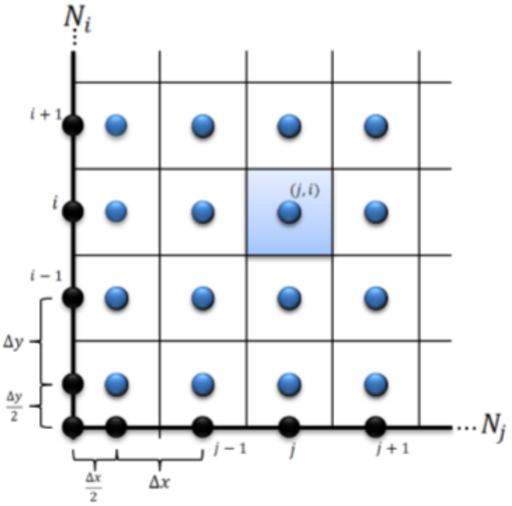

Fig. 3.4 *Illustration of the cell volume and the adjacent nodes. T_{n^+} and T_{n^-} denotes the phase values at the cell boundaries in negative and positive n-directions, $T_{n^{++}}$ and $T_{n^{--}}$ denotes the adjacent node values in the neighbouring cells.*

Integrating Eq (2.14) over the cell volume seen in Figure 3.4 yields:

$$\begin{aligned}&\int_{t^-}^{t^+}\int_{x^-}^{x^+}\int_{y^-}^{y^+}\int_{z^-}^{z^+} \rho c(T)\frac{\partial T}{\partial t}\,dtdxdydz = \\ &\int_{t^-}^{t^+}\int_{x^-}^{x^+}\int_{y^-}^{y^+}\int_{z^-}^{z^+} \nabla\cdot(k(T)\,\nabla T)\,dtdxdydz + \int_{t^-}^{t^+}\int_{x^-}^{x^+}\int_{y^-}^{y^+}\int_{z^-}^{z^+} S\,dtdxdydz\end{aligned} \tag{3.3}$$

LHS:

Evaluating the left hand side of Eq (3.3), and assuming constant density yields:

$$\int_{t^-}^{t^+}\int_{x^-}^{x^+}\int_{y^-}^{y^+}\int_{z^-}^{z^+} \rho c(T)\frac{\partial T}{\partial t}\,dtdxdydz \approx \left(cT\Big|_{t^+} - cT\Big|_{t^-} \right)\rho\Delta x\Delta y\Delta z \tag{3.4}$$

RHS:

Evaluating the right hand side of Eq (3.3), yields:

$$
\begin{gathered}
\int_{t^-}^{t^+}\int_{x^-}^{x^+}\int_{y^-}^{y^+}\int_{z^-}^{z^+} \nabla\cdot(k(T)\,\nabla\,T)\,dtdxdydz = \\
\underbrace{\int_{t^-}^{t^+}\int_{x^-}^{x^+}\int_{y^-}^{y^+}\int_{z^-}^{z^+} \frac{\partial}{\partial x}\left[k(T)\,\frac{\partial T}{\partial x}\right] dtdydz\,+}_{(1)} \\
\underbrace{\int_{t^-}^{t^+}\int_{x^-}^{x^+}\int_{y^-}^{y^+}\int_{z^-}^{z^+} \frac{\partial}{\partial y}\left[k(T)\,\frac{\partial T}{\partial y}\right] dtdxdz\,+}_{(2)} \\
\underbrace{\int_{t^-}^{t^+}\int_{x^-}^{x^+}\int_{y^-}^{y^+}\int_{z^-}^{z^+} \frac{\partial}{\partial z}\left[k(T)\,\frac{\partial T}{\partial z}\right] dtdxdy\,+}_{(3)} \\
\underbrace{\int_{t^-}^{t^+}\int_{x^-}^{x^+}\int_{y^-}^{y^+}\int_{z^-}^{z^+} S\,dtdxdydz}_{(4)}
\end{gathered}
\tag{3.5}
$$

Evaluating the terms (1), (2), (3) and (4) in Eq (3.5) individually, using the second order central difference scheme for the derivatives, explicit scheme in time, and a mean value of the conductivity yield:

(1):

$$
\begin{gathered}
\int_{t^-}^{t^+}\int_{x^-}^{x^+}\int_{y^-}^{y^+}\int_{z^-}^{z^+} \frac{\partial}{\partial x}\left[k(T)\,\frac{\partial T}{\partial x}\right] dtdydz \approx \\
\left[k\frac{\partial T}{\partial x}\bigg|_{x^+} - k\frac{\partial T}{\partial x}\bigg|_{x^-}\right]\Delta t\Delta y\Delta z \approx \\
\left[\left(\frac{k_{x^{++}}+k}{2}\right)\left(\frac{T_{x^{++}}-T}{\Delta x}\right)-\left(\frac{k+k_{x^{--}}}{2}\right)\left(\frac{T-T_{x^{--}}}{\Delta x}\right)\right]\bigg|_{t^-}\Delta t\Delta y\Delta z
\end{gathered}
\tag{3.6}
$$

A similar procedure can be conducted for term (2) and (3) in Eq (3.5). Evaluating term (4) yields:

$$
\int_{t^-}^{t^+}\int_{x^-}^{x^+}\int_{y^-}^{y^+}\int_{z^-}^{z^+} S\,dtdxdydz \approx \overline{S}\,\Delta t\Delta x\Delta y\Delta z \tag{3.7}
$$

Adding Eq (3.4) and Eq (3.7), together with the similar expressions for the y- and z-direction, we arrive at the fully discretized transient heat equation. Eq (3.8).

$$\begin{aligned}
&\left(cT\Big|_{t^+} - cT\Big|_{t^-}\right)\rho\Delta x\Delta y\Delta z = \\
&\left[(\frac{k_{x^{++}}+k}{2})(\frac{T_{x^{++}}-T}{\Delta x}) - (\frac{k+k_{x^{--}}}{2})(\frac{T-T_{x^{--}}}{\Delta x})\right]\Bigg|_{t^-}\Delta t\Delta y\Delta z \quad + \\
&\left[(\frac{k_{y^{++}}+k}{2})(\frac{T_{y^{++}}-T}{\Delta y}) - (\frac{k+k_{y^{--}}}{2})(\frac{T-T_{y^{--}}}{\Delta y})\right]\Bigg|_{t^-}\Delta t\Delta y\Delta z \quad + \\
&\left[(\frac{k_{z^{++}}+k_z}{2})(\frac{T_{z^{++}}-T}{\Delta z}) - (\frac{k+k_{z^{--}}}{2})(\frac{T-T_{z^{--}}}{\Delta z})\right]\Bigg|_{t^-}\Delta t\Delta x\Delta y \quad + \\
&\overline{S}\,\Delta t\Delta x\Delta y\Delta z
\end{aligned} \tag{3.8}$$

3.5.5 Source term

The energy input from the laser per node, Q_{inp} is equal to $\overline{S}\Delta x\Delta y\Delta z$, and is dependent upon the overall exposure of the nodes to the laser. In this thesis, there are three different cases of power inputs, namely P_1, P_2 and P_3, i.e. the power input to "shaded nodes", "fully exposed nodes" and "partially shaded nodes".

$$Q_{inp} = \begin{cases} P_1 = 0, & \textit{for}\text{ shaded nodes} \\ P_2 = \frac{P_l - P_r}{n_l}, & \textit{for}\text{ fully exposed nodes} \\ P_3 = \frac{P_l - P_r - P_w - P_2 \cdot n_{fen}}{n_{psn}}, & \textit{for}\text{ partially shaded nodes} \end{cases} \tag{3.9}$$

where P_l is the power input from the laser, P_w is the power to the wire, n_l is the number of nodes under the laser, n_{psn} is the number of partially shaded nodes, and n_{fen} is the number of fully exposed nodes.

3.5.6 Boundary conditions implementation

3.5.6.1 Fluid-solid boundary

Figure 3.5 illustrates the fluid-solid boundary of the discretized domain, i.e. the boundary between the substrate/air, and deposited layer/air. The boundary temperature T_b is a function of the internal temperature closest to the boundary, T_1, and the surrounding temperature of the fluid, T_f.

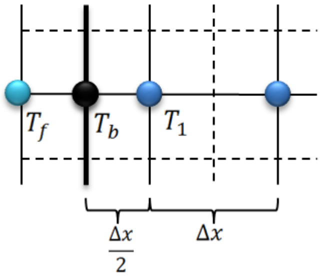

Fig. 3.5 *Illustration of the (solid-fluid) boundary nodes, where T_f is the temperature of the fluid, T_b the temperature of the boundary node, and T_1 is the temperature of the internal node closest to the boundary.*

The boundary condition, Eq (2.23), is highly nonlinear. In this work the boundary condition is simplified to obtain a linear boundary condition. Eq (2.22) is therefor linearized. This is done by simply using the temperature value from the previous time step $T(t^-)$:

$$h_{rad} = \sigma\epsilon(T_b(t^-)^2 + T_f^2)(T_b(t^-) + T_f) \tag{3.10}$$

Thus, Eq (2.23) becomes:

$$-k\frac{T_b(t) - T_1}{\Delta x/2} = \left[\epsilon\sigma(T_b(t^-)^2 + T_f^2)(T_b(t^-) + T_f) + h_{conv}\right](T_b(t^+) - T_f) \tag{3.11}$$

To simplify the problem, a conductive heat transfer coefficient is introduced:

$$h_{cond} = k/(\Delta x/2) \tag{3.12}$$

Eq (3.11) becomes:

$$-h_{cond}(T_b(t) - T_1) = (h_{rad} + h_{conv})(T_b(t) - T_f) \tag{3.13}$$

Solving for the value of T_b of the current time step, i.e $T_b(t)$ in Eq (3.11), yields the expression:

$$T_b(t) = \frac{(h_{rad} + h_{conv}) \cdot T_f + h_{cond} \cdot T_1}{h_{rad} + h_{conv} + h_{cond}} \tag{3.14}$$

3.5.6.2 Solid-solid boundary

Figure 3.6 illustrates the solid-solid boundary, i.e the boundary between the substrate and the deposited bed, and between the strings, depending if the string are deposited next to each other. T_1 and T_2 are the temperatures of the internal nodes in the two solids closest to the boundary, and T_b is the temperature of the boundary node.

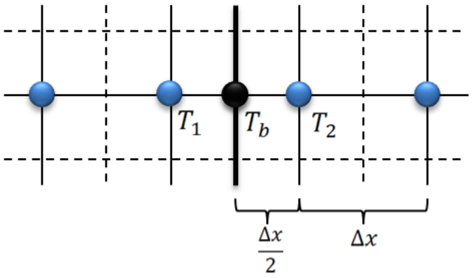

Fig. 3.6 *Illustration of the (solid-solid) boundary nodes, where T_1 and T_2 is the temperature of the two solids, and T_b is the temperature of the boundary node.*

Discretizing Eq (2.24) yields:

$$k_1\frac{(T_1 - T_b(t))}{\Delta x/2} = k_2\frac{(T_b(t) - T_2)}{\Delta x/2} \tag{3.15}$$

Introducing h^{-}_{cond} and h^{+}_{cond} as:

$$h^1_{cond} = \frac{k_1}{\Delta x/2} \tag{3.16}$$

$$h^2_{cond} = \frac{k_2}{\Delta x/2} \tag{3.17}$$

And solving for $T_b(t)$ in Eq (3.15) yields:

$$T_b(t) = \frac{h^1_{cond}\cdot T_1 + h^2_{cond}\cdot T_2}{h^1_{cond} + h^2_{cond}} \tag{3.18}$$

3.5.7 Algorithm

The fundamental construction of the algorithm is shown below. Note, that the algorithm presented is merely a short summary. The discretized form of the heat equation Eq (3.8), is used to find the heat content in each node. As the mass of the nodes are known in the top and lower domain, the heat content per unit mass can be found. Eq (2.13) is discretized in the interval $0 < T < T_{bTi}$, which gives the heat content per unit mass as a function of temperature, see Figure 2.5. Thus, the temperature can be found, and the latent heat of fusion and vaporization is taken into account.

Algorithm 1 Simulation approach

```
Input parameters: Apply values to the parameters described in Table 3.1.
Initialise Data: Initialisation of material properties, temperature matrices, and heat correlations.
Initial calculations: Heat input, mass per node, layer height, number of shaded nodes and partially shaded nodes, time steps etc.
counter node = 1                                        ▷ initialise counter
counter string = 1
counter layer = 1
for counter = 1 : steps do                              ▷ steps = number of time steps
    if counter > steps per node * counter node then
        - Move the laser one node and activate mass and material properties
        - Save deposited nodes                          ▷ to keep track on deposited nodes
    else
        - Within pause interval, shut off laser and stay at current nodes.
        - counter node = counter node +1
    end if
    if counter > steps per string * counter string then
        - Move the laser to next string
        - Save string nodes
        - counter string = counter string + 1
    end if
    if counter > steps per layer * counter layer then
        - Move the laser to the next layer
        - Save layer nodes
        - counter layer = counter layer + 1
    end if
    Reset matrices: Reset matrices and calculate new delta temperatures and average heat conductivity between adjacent nodes.
    Implement boundary conditions: Implement Eq (3.5) and Eq (3.6)
    Calculate temperature: Eq (3.8) gives the heat content in each node, from this information the temperature is found by interpolation, see Figure 2.5.
    if counter string > 1 then
        Perform calculation for previous strings
    end if
    if counter layer > 1 then
        Perform calculation for previous layer
    end if
    Power input: Calculate the power input to the nodes $Q_{inp}$
    Temperature dependent parameters: Calculate new values for $\epsilon$ and $k$.
end for
```

4

Results & Analysis

This chapter includes the results from the comparisons of experimental data with simulation data, the sensitivity analysis and the DOE. The accuracy measurements are simulated with the best settings received from the sensitivity analysis. The results are followed by brief discussions and analysis. Note that the temperature in the figures has been scaled with T_0, and does therefore not represent the real temperatures.

4.1 Model accuracy

Figure 4.1 shows the temperature versus time at the locations of the thermocouples Tc_1, Tc_2, Tc_3 and Tc_4 for process trial E_1, and the data received from the simulations in the same positions as the four thermocouples. The vertical lines intersect the time-axis in, 164, 333, 490 and 670 seconds, time-coordinates that represent the start of a new layer.

The maximum temperature deviation occurs in the Tc_1 position at 138 seconds, with a deviation of 30 %. This is because the simulated temperature rises too quickly, approximately one second earlier than the experimental value. The deviation is evened up at 139 seconds, with a temperature difference of approximately 1%.

As the laser is right above Tc_4 after 72 seconds, this point can serve as an indicator of the accuracy of the local melt pool temperature, see Figure 4.1d. The temperature deviation at 72 seconds is 0.5 %, which indicates that the local temperature is accurate. As the laser do not traverse over the thermocouple Tc_1, Tc_2 and Tc_3, these can be seen as indicators of global temperature accuracy rather than a measure of local temperature accuracy.

Table 4.1: Minimum and maximum temperature deviations, ΔT_{max} and ΔT_{min}, in the positions of thermocouples Tc_1, Tc_2, Tc_3 and Tc_4 for E_1.

Thermocouple	ΔT_{max}	ΔT_{min}
Tc_1	30 % , 138 s	$>$ 1 % , 99 s
Tc_2	20 %, 138 s	$>$ 1 %, 277 s
Tc_3	19 % , 138 s	$>$ 1 % , 3 s
Tc_4	10 %, 42 s	$>$ 1 % , 35 s

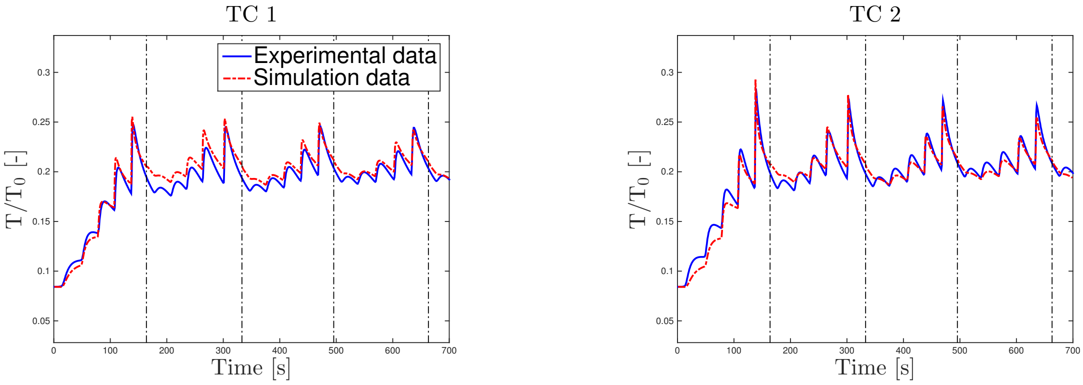

(a) *Experimental and simulation values of temperature at Tc_1 vs time.*

(b) *Experimental and simulation values of temperature at Tc_2 vs time.*

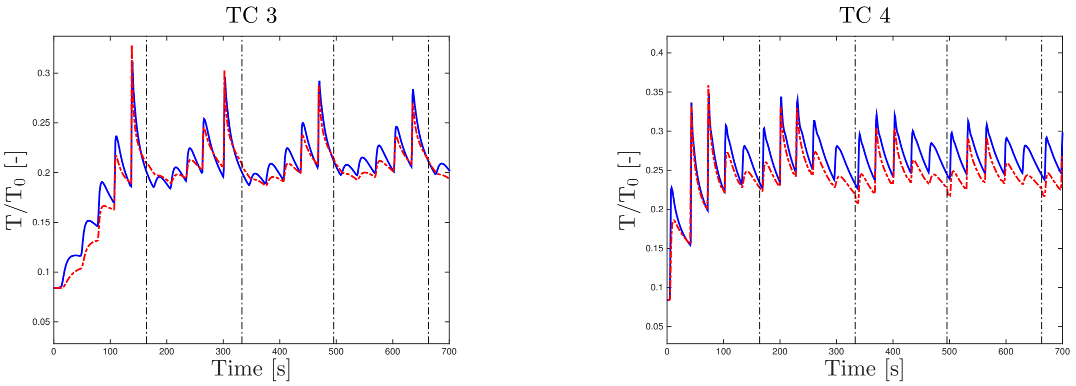

(c) *Experimental and simulation values of temperature at Tc_3 vs time.*

(d) *Experimental and simulation values of temperature at Tc_4 vs time.*

Fig. 4.1 *Comparison of experimental and simulation temperature values in a 700 seconds interval at the positions of Tc_1 (a), Tc_2 (b), Tc_3 (c) and Tc_4 (d) from process trial E_1.*

Figure 4.2 shows the temperature versus time at the locations of the thermocouples Tc_1, Tc_2, Tc_3 and Tc_4 for E_2, and data received from the simulations. In this experiment, a long pause time after the deposition of the second string has been used. This can be seen by the exponentially declining temperature, approximately 50 % from the end of string two at 67 seconds, to the start of string three at 700 seconds.

The agreement of the simulation data and the experimental data is satisfying. The overall frequency, as well as maximum and minimum values coincides. This indicates that the algorithm used does not include serious bugs or errors. The maximum temperature deviation occurs after four seconds in the position of Tc_3 with a value of 40 %. This is also due to the curves being slightly out of phase, and as a result, the simulation value rises two seconds earlier than the experimental value.

Table 4.2: Minimum and maximum temperature deviations, ΔT_{max} and ΔT_{min}, in the positions of thermocouples Tc_1, Tc_2, Tc_3 and Tc_4 for E_2

Thermocouple	ΔT_{max}	ΔT_{min}
Tc_1	25 %, 4 s	< 1 %, 325 s
Tc_2	32 %, 24 s	< 1 %, 308 s
Tc_3	42 %, 3 s	< 1 %, 328 s
Tc_4	15 %, 25 s	< 1 %, 326 s

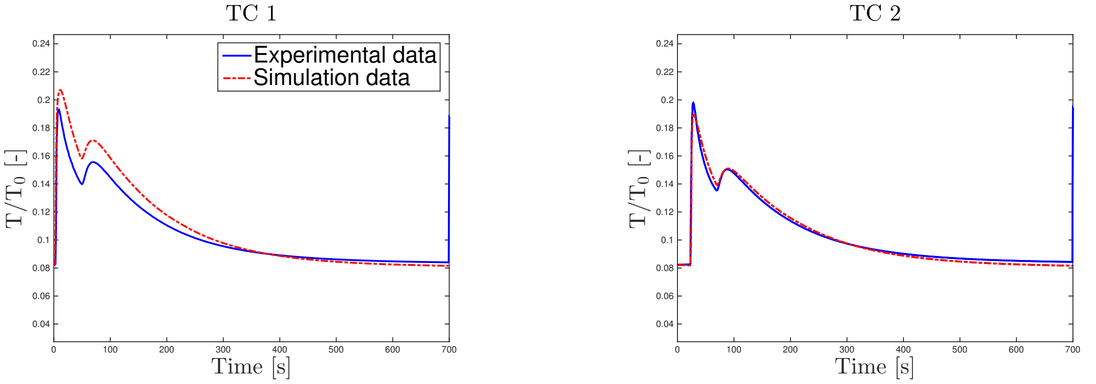

(a) *Experimental and simulation values of temperature at Tc_1 vs time.*

(b) *Experimental and simulation values of temperature at Tc_2 vs time.*

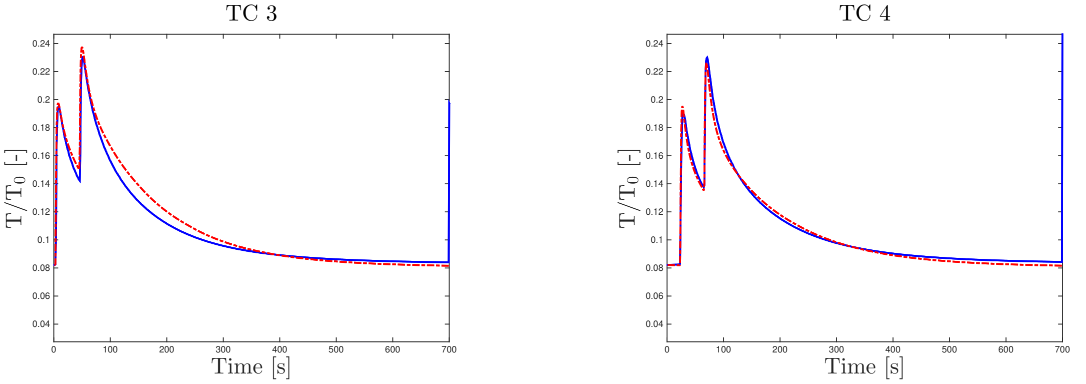

(c) *Experimental and simulation values of temperature at Tc_3 vs time.*

(d) *Experimental and simulation values of temperature Tc_4 vs time.*

Fig. 4.2 *Comparison of experimental and simulation temperature values in a 700 seconds interval at the positions of Tc_1 (a), Tc_2 (b), Tc_3 (c) and Tc_4 (d) from process trial E_2.*

4.2 Sensitivity analysis numerical parameters

In this section, the sensitivity analysis of the the grid spacing and time step size are presented.

4.2.1 Size of time step

Figure 4.3 illustrates the results received from the simulations using different values of the time step size t_s. Using Eq (2.20), a stable t_s was found to be approximately 0.0017 seconds. The simulations diverged for a time step of 0.0020 seconds, which confirms the validity of Eq (4.3). From Figure 4.8 it can be observed that a decrease in time step size does not alter the solution significantly, globally or locally.

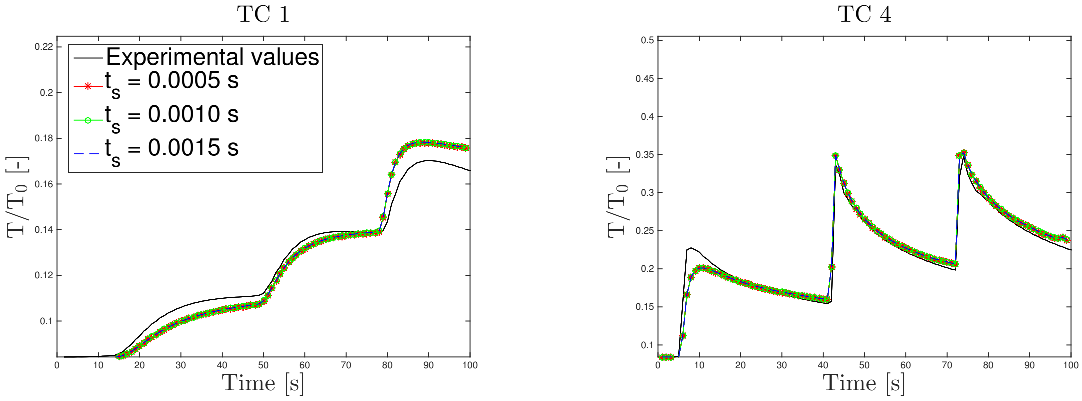

(a) *Tc_1 vs time for time steps equal to 0.0005 s, 0.0001 s and 0.00015 s.*

(b) *Tc_4 vs time for time steps equal to 0.0005 s, 0.0001 s and 0.00015 s.*

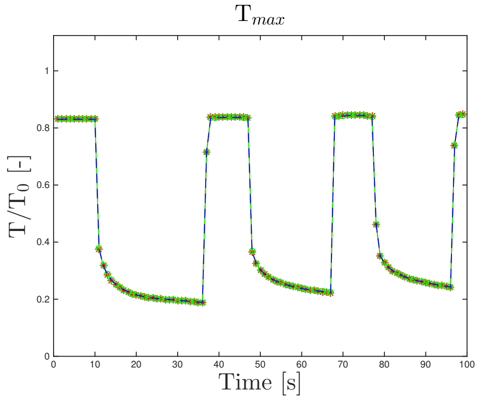

(c) *T_{max} vs time for time steps equal to 0.0005 s, 0.0001 s and 0.00015 s.*

Fig. 4.3 *Results from the sensitivity analysis of different values of the time stepping at the locations of the thermocouples Tc_1 (a), Tc_4 (b), and for the maximum temperature T_{max} (c).*

4.2.2 Size of substrate grid spacing

Figure 4.4 illustrates the results received from the simulations using different values of the grid spacing of the substrate Δx. In Figure 4.4c, the maximum temperature drops approximately 5 % when using a Δx of 0.3 mm compared to 0.5 mm. Figure 4.4a reveals that the smaller the Δx, the larger the cooling rate becomes. This is especially true in the interval of 85 seconds to 100 seconds. This clearly indicates that the solution is not grid independent. For low global temperatures, grid spacings of 1.0 mm gives equal readings compared to 0.5 and 0.3 mm grid spacings. As described in section 2.5.1, the central difference scheme used when approximating the derivatives is second order accurate. Thus, the error increases with an exponential factor of two with increased grid spacing. Unfortunately, the results presented in Figure 4.4 is contradictory to this fact as a grid spacing of 0.3 mm worsen the accuracy with respect to experimental data. The results indicate that using larger grid spacings require larger heat transfer coefficients to produce accurate results. However, this also indicates that using a lower Δx could lower the heat transfer coefficient down to more reasonable values.

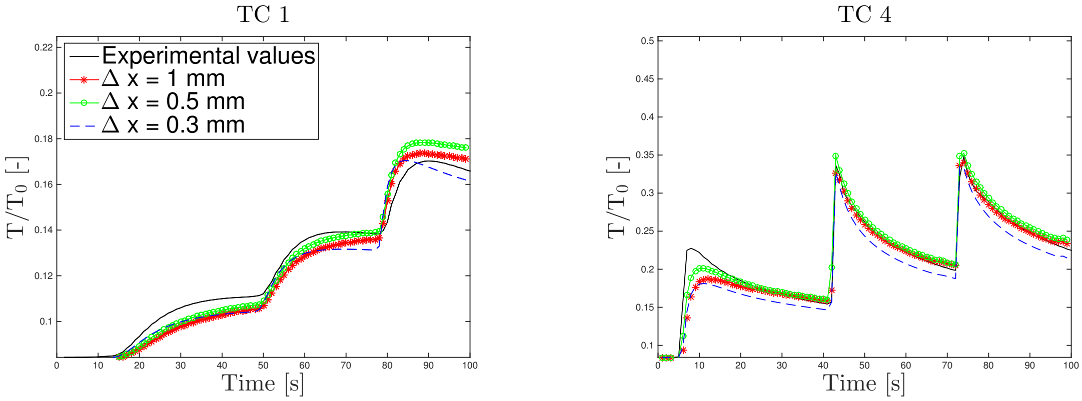

(a) *Tc_1 vs time for substrate grid spacing equal to 0.3, 0.5 and 1 mm.*

(b) *Tc_4 vs time for substrate grid spacing equal to 0.3, 0.5 and 1 mm.*

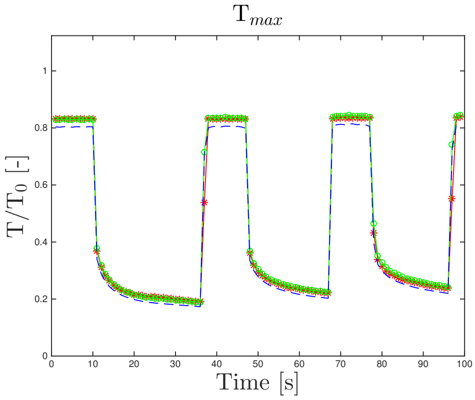

(c) *T_{max} vs time for substrate grid spacing equal to 0.3, 0.5 and 1 mm..*

Fig. 4.4 *Results from the sensitivity analysis of different values of the substrate grid spacing at the locations of the thermocouples Tc_1 (a), Tc_4 (b), and for the maximum temperature T_{max} (c).*

The simulation time is clearly dependent upon the number of nodes, as the number of calculations needed increases with each new node. Table 4.3 shows the simulation time for the different grid spacings. The simulation time is expressed in minutes of simulation time per second of deposition min/s.

Table 4.3: Simulation time and number of nodes for a substrate grid spacing of 0.3 mm, 0.5 mm and 1.0 mm.

Δx	Number of nodes	Simulation time
0.3 mm	1562850	5 min/s
0.5 mm	453180	1 min/s
1.0 mm	92000	0.15 min/s

4.3 Sensitivity analysis thermo parameters

In this section, the results from the sensitivity analysis of thermodynamical parameters, as well as geometrical parameters are presented.

4.3.1 Heat transfer coefficient

Figure 4.5 illustrates the results received from the simulations using different values of the heat transfer coefficient h. By using the relations described in section 2.2.3, the heat transfer coefficient for natural convection was found. This value is set to the nominal value, i.e. 100 %. As can be observed from Figure 4.5, the most accurate results is given for h = 1000 %. To generate such a heat transfer coefficient would require a fluid velocity of around 20 m/s, which was found by using correlations for forced convection. This could indicate that there is an error in the way the boundary conditions is implemented. Thus the heat transfer coefficient may be compensating for a too low radiative heat transfer coefficient. The results illustrated in Figure 4.5 indicate that a heat transfer coefficient corresponding to that in natural convection, is too small. It is also observed, that the heat transfer coefficient has a larger impact on the accuracy of the global temperature, than on the local temperature because the deviation in Figure 4.5a is larger than in that of Figure 4.5b.

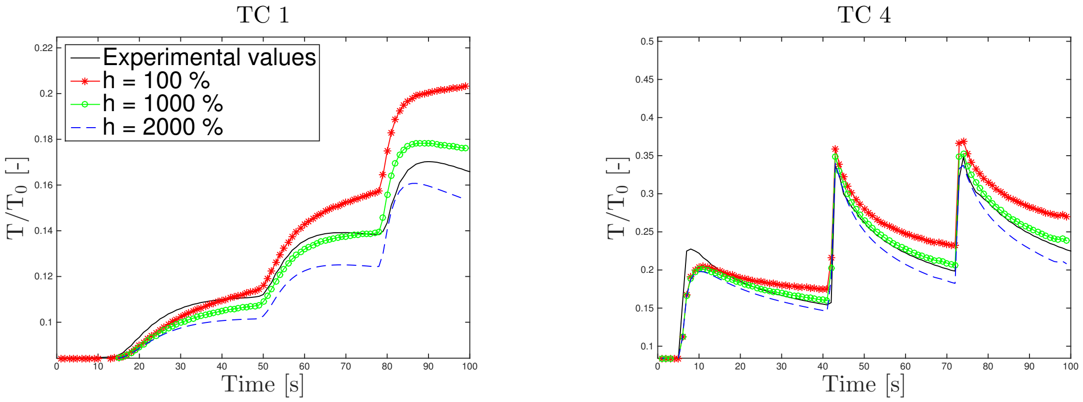

(a) *Tc_1 vs time for heat transfer coefficients equal to 100 %, 1000 % and 2000 %.*

(b) *Tc_4 vs time for heat transfer coefficients equal to 100 %, 1000 % and 2000 %..*

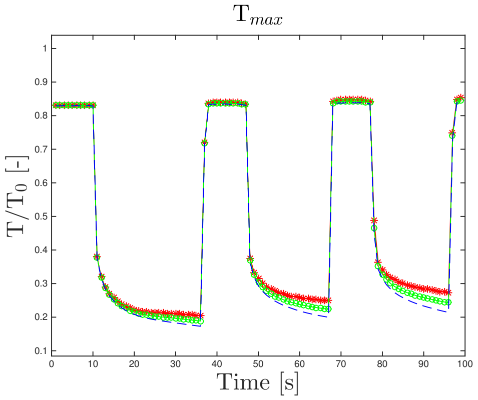

(c) *T_{max} vs time for heat transfer coefficients equal to 100 %, 1000 % and 2000 %.*

Fig. 4.5 *Results from the sensitivity analysis of different values of the heat transfer coefficient at the locations of the thermocouples Tc_1 (a), Tc_4 (b), and for the maximum temperature T_{max} (c).*

4.3.2 Reflectivity

Figure 4.6 illustrates the results received from the simulations using different values of the reflectivity r. The value of r has a large impact on the maximum temperature, as well as the overall temperature in the domain. This is due to the parameter's direct impact on the amount of incident power reaching the substrate and deposited layers.

The reflectivity is dependent upon the frequency of the light source and the temperature of the material, and for metals, in case of normal incidence, the reflection coefficient for near ultra violet radiation and visible light is around 0.4-0.9. The results observed in Figure 4.6 indicates that an optimum value for the reflection coefficient is around 0.5. Too small reflection (around 10 %) causes the melt pool temperature to reach the boiling temperature of Ti64.

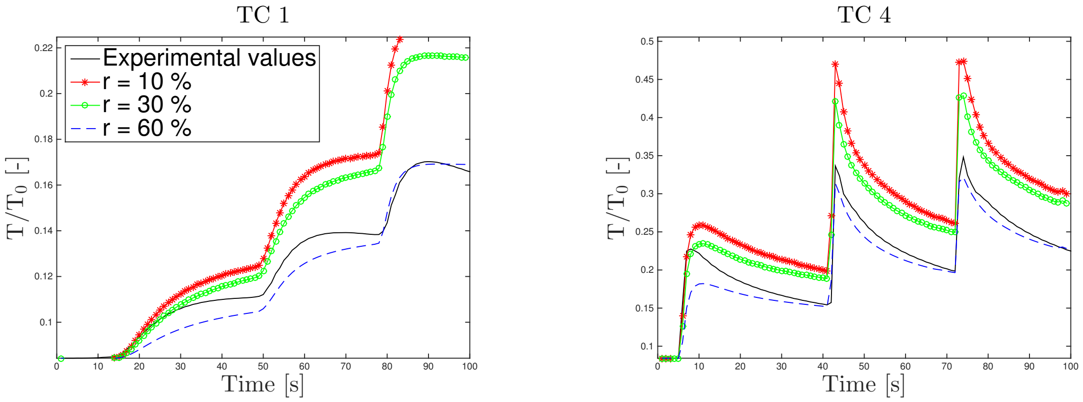

(a) *Tc_1 vs time for reflection coefficients equal to 10 %, 30 % and 60 %.*

(b) *Tc_4 vs time for reflection coefficients equal to 10 %, 30 % and 60 %.*

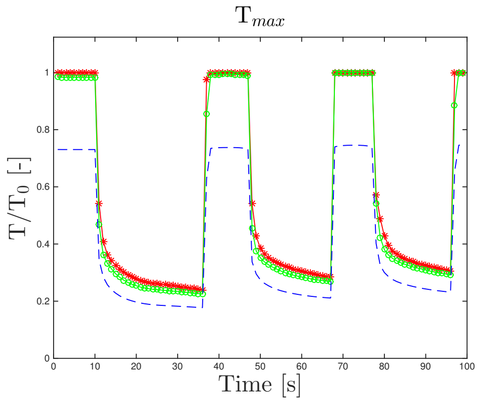

(c) *T_{max} vs time for reflection coefficients equal to 10 %, 30 % and 60 %.*

Fig. 4.6 *Results from the sensitivity analysis of different values of the reflection coefficient at the locations of the thermocouples Tc_1 (a), Tc_4 (b), and for the maximum temperature T_{max} (c).*

4.3.3 Ambient temperature

Figure 4.7 illustrates the results received from the simulations using different values of the ambient temperature T_a. As the radiation and convective heat transfer is directly dependent upon the ambient temperature, it is clear that the rate of cooling will be affected by this parameter. However, according to the results in Figure 4.7, the change is negligible, especially for higher temperatures, see Figure 4.7c.
A change in temperature from 295 K to 400 K will change the heat flux from the surface of a temperature of 2000 K by approximately 1 %. Even at lower temperatures, the heat flux is still too small to affect the surface temperature to a greater extent.

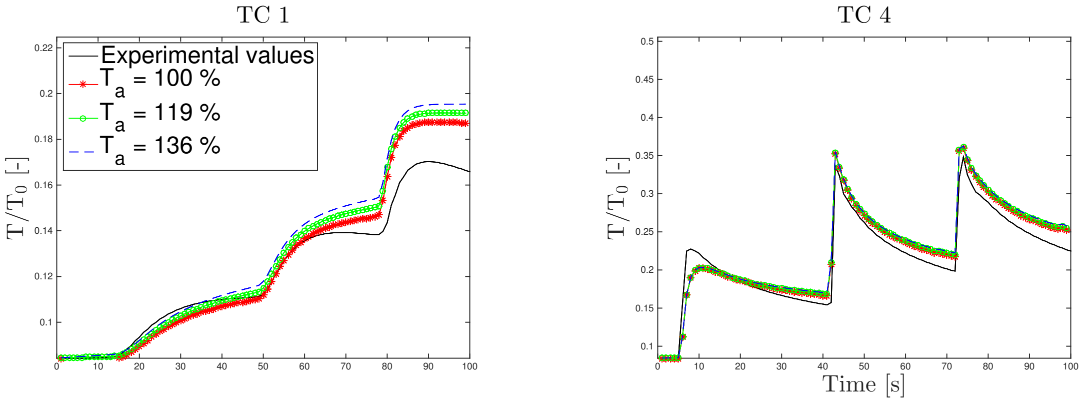

(a) *Tc_1 vs time for ambient temperatures equal to 100 %, 119 % and 136 %.*

(b) *Tc_4 vs time for ambient temperatures equal to 100 %, 119 % and 136 %.*

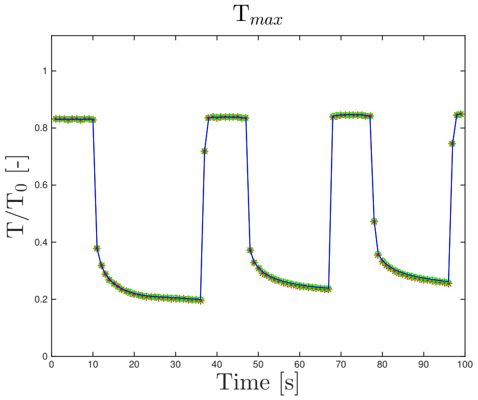

(c) *T_{max} vs time for ambient temperatures equal to 100 %, 119 % and 136 %.*

Fig. 4.7 *Results from the sensitivity analysis of different values of the ambient temperature at the locations of the thermocouples Tc_1 (a), Tc_4 (b), and for the maximum temperature T_{max} (c).*

4.3.4 Wire temperature

Figure 4.8 illustrates the results received from the simulations using different values of the wire temperature T_w. The energy that reaches the substrate through the melted wire is equal to the initial energy of the wire, plus the energy the wire absorbs during the time it is exposed to the laser. The increased heat that reaches the substrate via the melted wire when increasing the wire temperature to 136 % of the nominal value, is approximately only 0.2 % of the heat input coming from the laser. Thus, the wire temperature is negligible compared to the overall power input from the laser. This is confirmed by the results in Figure 4.8 as the curves coincides regardless of the wire temperature.

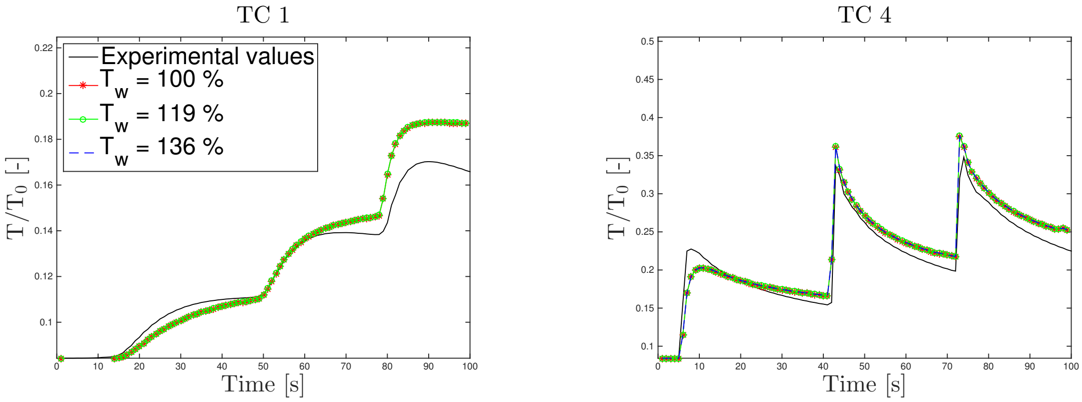

(a) *Tc_1 vs time for ambient temperatures equal to 100 %, 119 % and 136 %.*

(b) *Tc_4 vs time for ambient temperatures equal to 100 %, 119 % and 136 %.*

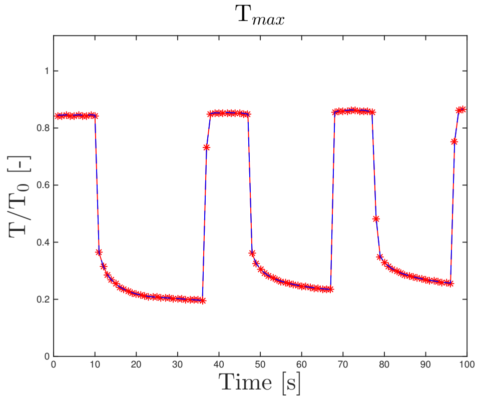

(c) *T_{max} vs time for ambient temperatures equal to 100 %, 119 % and 136 %.*

Fig. 4.8 *Results from the sensitivity analysis of different values of the wire temperature at the locations of the thermocouples Tc_1 (a), Tc_4 (b), and for the maximum temperature T_{max} (c).*

4.3.5 Thickness of substrate

Figure 4.4 illustrates the results received from the simulations using different values of the substrate thickness s_t in percentage of nominal thickness. From Figure 4.4 it can be observed that the overall temperature at the thermocouples increases for decreasing thickness. The maximum temperature is unaffected during the peaks, as can be observed from Figure 4.9c. However, for the lower maximum temperature values (when the laser is switched off) the difference is more noticeable. Increasing the substrate thickness from 83 % to 117 % of the nominal value decreases the temperature at the bottom of the substrate (right under the laser) by approximately 26 %. Thus, the overall cooling effect by increasing the thickness is substantial and more noticeable at higher temperatures. This is a reasonable consequence since increasing the substrate thickness, the mass of the substrate will increase, and hence, more energy can be stored.

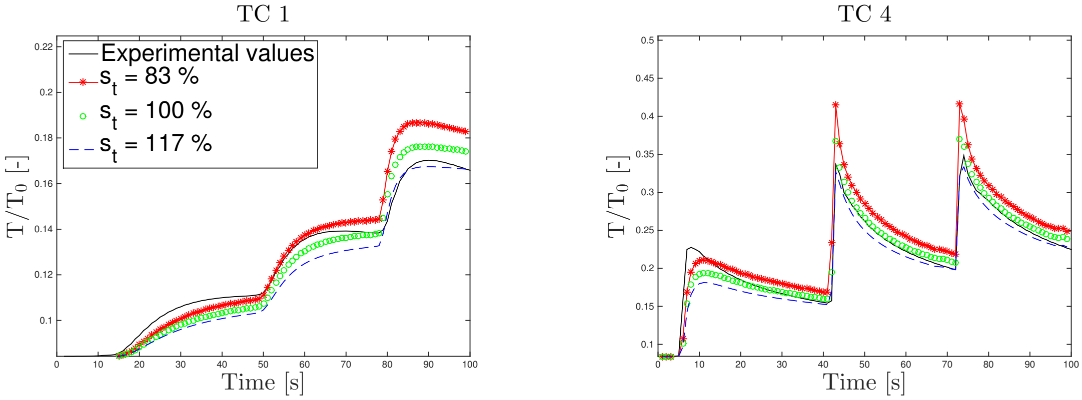

(a) *Tc_1 vs time for substrate thickness of 83 %, 100 % and 117 %*

(b) *Tc_4 vs time for substrate thickness of 83 %, 100 % and 117 %*

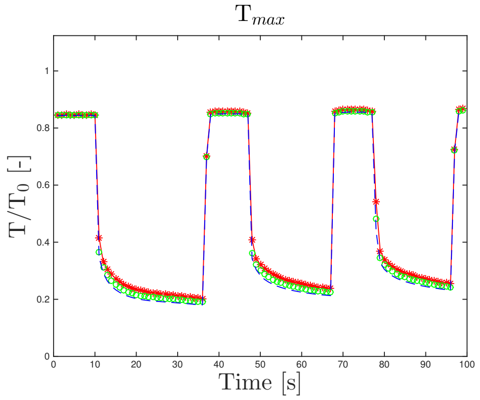

(c) *T_{max} vs time for substrate thickness of 83 %, 100 % and 117 %*

Fig. 4.9 *Results from the sensitivity analysis of different values of the substrate thickness at the locations of the thermocouples Tc_1 (a), Tc_4 (b), and for the maximum temperature T_{max} (c).*

4.3.6 Thermocouple placement

Figure 4.10 illustrates the results received from the simulations using different x-coordinates for the placing of the thermocouples. Note that the laser traverses in the positive x-direction.

The coordinates of the thermocouples in the simulations has a profound effect on how the simulation values deviates from the experimental values. The maximum temperature deviation between the thermocouple positions placed +2 mm and -2 mm from the original position is approximately 8 %, see Figure 4.10a at 85 seconds. The temperature at Tc_1 increases with decreasing x-direction and vice verse. The reason is that the thermocouple is moved closer to the heat source when moving in the negative x-direction, and further away when moving in the positive x-direction. Changing the positions in x-direction also results in a phase change, i.e. an offset of the heat source peak. However, in this case, the phase change is negligible because of the high traverse speed relative to the length of the studied thermocouple displacement.

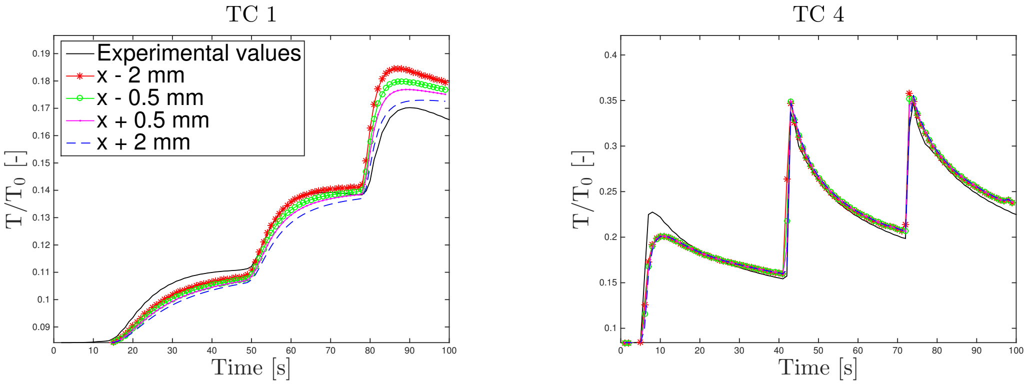

(a) *Tc_1 vs time for thermocouple displacement in the x-direction by ±0.5 and ±2 mm from original position.*

(b) *Tc_4 vs time for thermocouple displacement in the x-direction by ±0.5 and ±2 mm from original position.*

Fig. 4.10 *Results from the sensitivity analysis of different values of the thermocouple displacement in x-direction at the locations of the thermocouples Tc_1 (a) and Tc_4 (b).*

Figure 4.11 shows the results received from the simulations using different y-coordinates for the placing of the thermocouples. The y-direction is perpendicular to the traverse direction.

The displacing of the thermocouples in y-direction has larger impact on the temperature in Tc_4, with a maximum deviation of 34 % at 73 seconds, see Figure 4.11b. The explanation lies in the large temperature gradients near the centre of the heat source that causes temperature deviations of approximately 10-15% per mm of displacement. Tc_1 is also moved closer to the heat source in negative y-direction, thus explaining the increased temperature.

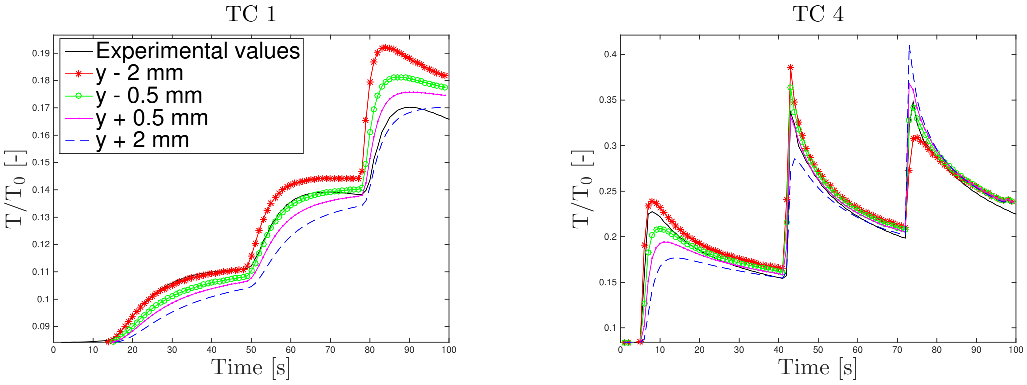

(a) *Tc_1 vs time for thermocouple displacement in the y-direction by ±0.5 and ±2 mm from original position.*

(b) *Tc_4 vs time for thermocouple displacement in the y-direction by ±0.5 and ±2 mm from original position.*

Fig. 4.11 *Results from the sensitivity analysis for different values of the thermocouple displacement in y-direction at the locations of the thermocouples Tc_1 (a) and Tc_4 (b).*

4.4 DOE results

In this section, the results from the DOE are presented. Note that the axes in the figures have been scaled, and do therefore not represent the real dimensions and temperatures.

4.4.1 Temperature distributions

The temperature distribution was simulated with the nominal values of the process parameters, i.e. Laser power 100 %, wire feed rate 100%, traverse speed 100 %, pause times 100 % and front feeding. Figure 4.12a illustrates the temperature distribution in a cross sectional segment spanning through the middle of the deposited layer and the substrate after 215 seconds of deposition. The vertical axis, z/D_0 represents the thickness and the horizontal axis x/D_0 represents the length in the traverse direction. At this point in time, two layers, each with three strings have been deposited, and the third layer is half way trough its deposition. The heat source creates a melt pool with very high temperature gradients in and close to it. The maximum temperature is achieved directly under the laser, at the edge of the newly deposited layer. The traverse speed is comparably faster than the conductive flow of heat, which causes a "temperature wall", seen at $x/D_0 = 20$, that moves with the traverse speed in the positive x-direction. The temperature increase at the edge of the "temperature wall" is approximately 7 % per unit length up in the top of the domain, and approximately 1.2 % per unit length in the lower parts of the substrate. Figure 4.12b illustrates the temperatures alongside the x-direction at different positions in the z-direction, with a fixed y-value such as the temperature node is directly under the laser path after 35 seconds of deposition. Horizontal lines represents the temperature of the deposited wire, and the critical temperature limits Tk_0, Tk_1, Tk_2, and Tk_3. The temperature at the top of the substrate has two peaks, one of lower temperature due to the wire shading, and one of higher temperature due to no shading. In Figure 4.12b, outside the interval of $15 < x/D_0 < 22$, the temperature is approximately the same in the top, middle and bottom of substrate, and decreases linearly.

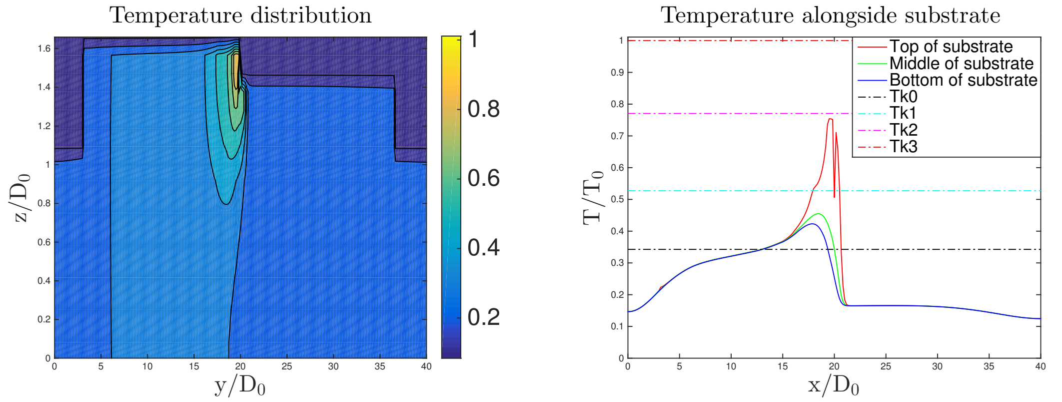

(a) *A contour plot of the temperature distribution in a cross sectional segment after 215 seconds of deposition.*

(b) *Temperature alongside the bed at different depths in the substrate after 35 seconds of deposition.*

Fig. 4.12 *Contour plot of the temperature distribution in a cross sectional segment (a), and the temperature alongside the bed at different depths in the substrate (b).*

Figure 4.13a illustrates the temperature distribution after 71 seconds of deposition. At this point, the first layer is deposited, and as the pause time starts, the laser is shut off. This explains the absence of a heat source. As the laser sweeps from left to right, down to up, the temperate are approximately 38 % higher in the top right, than in the bottom left when the pause times starts. As observed, the distribution of energy is limited to the deposited strings that now constitutes the layer. These nodes are activated, while the surrounding inactive nodes have a constant prescribed temperature.

Figure 4.13b illustrates the temperature distribution on top of the newly deposited layer after 215 seconds of deposition. As described above, the second string of the third layer is half way through its deposition at this point in time. The first deposited string works as a heat sink for the second deposited string, and the energy from the melt pool is spreading uniformly into this area. The high temperature area seen at $x/D_0 = 20$ is half of the actual width, since half of the laser is outside the edge of the newly deposited nodes.

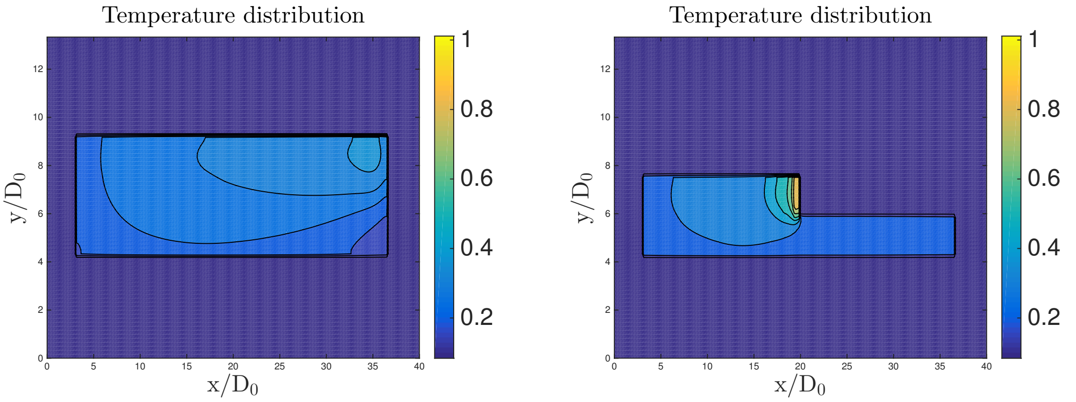

(a) *A contour plot of the temperature distribution on top of the newly deposited layer after 71 seconds of deposition.*

(b) *A contour plot of the temperature distribution on top of the newly deposited layer after 215 seconds of deposition.*

Fig. 4.13 *Contour plots of the temperature distribution on top of the newly deposited layer after 71 seconds (a), and 215 seconds (b) of deposition.*

Figure 4.14a shows the temperature distribution after 35 seconds of deposition. At this point, the second string of the first layer is halfway through its deposition. Due to the first deposited string which acts as a heat sink, the heat distribution is slightly displaced with higher temperatures in the negative y-direction. Figure 4.14 shows the temperature distribution on top of the substrate after 215 seconds. The temperature is now shifted to the lower parts of the domain, also due to the first deposited string in the third layer. Comparing Figure 4.14a-4.14b, the overall temperature (away from the laser source) has increased by approximately 60 % over the 220 seconds of deposition.

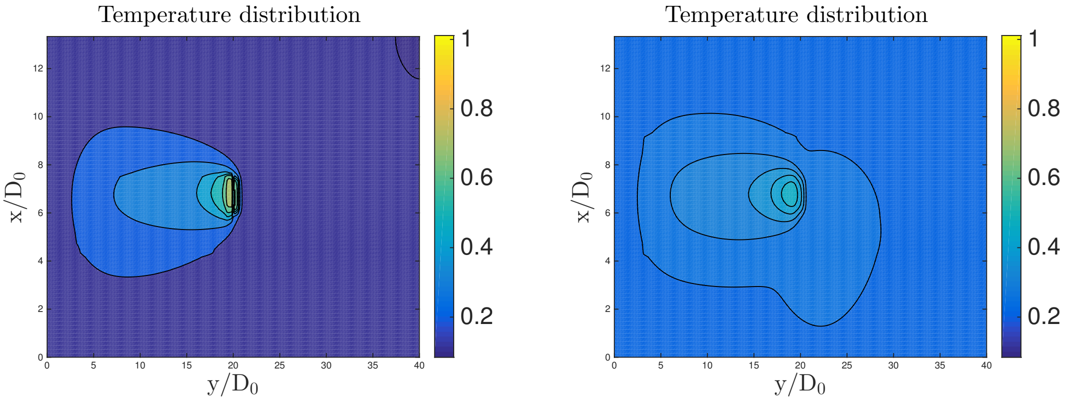

(a) *A contour plot of the temperature distribution on top of the substrate after 35 seconds of deposition.*

(b) *A contour plot of the temperature distribution on top of the substrate after 215 seconds of deposition.*

Fig. 4.14 *Contour plots of the temperature distributions on top of the substrate after 35 seconds (a), and after 214 seconds (b) of deposition.*

Figure 4.15a illustrates the temperature distribution on top of the substrate close to the heat source after 1 *s* of deposition. As the first layer is being deposited on top of the substrate at this point in time, both the deposited nodes and the substrate is partly exposed to the laser. Depending on the feeding direction, either the top layer, or the top of the substrate will be shadowed. As observed in Figure 4.15a the substrate is partly shaded by the wire due to front feeding, which creates an absence of power input near $(x/D_0, y/D_0)$=$(6.5, 5.25)$. This can be compared with Figure 4.15b where the wire instead shadows the top of the deposited layer, which greatly increases the temperature on the opposite side of the $x/D_0 = 6.5$. The reason why the maximum temperature in Figure 4.15a is not the same as in Figure 4.15b, is because the substrate is being directly exposed in the latter case.

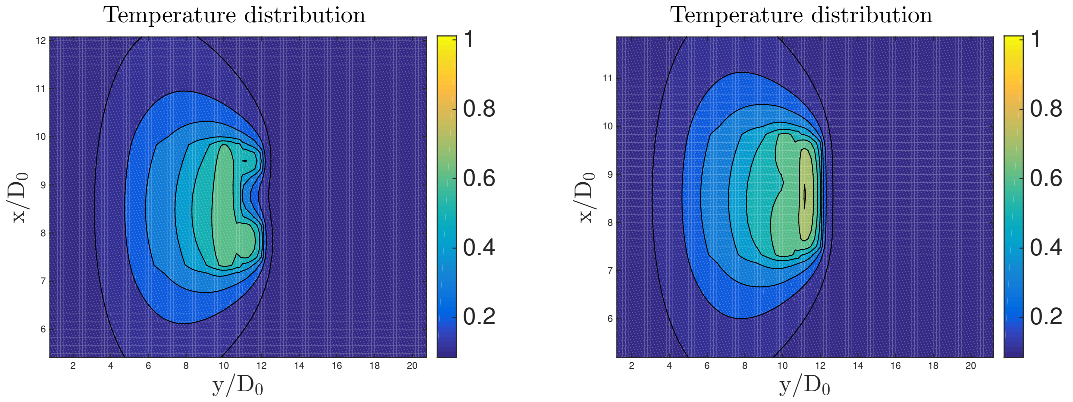

(a) *A zoomed in contour plot of the temperature distribution at the top of the substrate near the heat source using front feeding*

(b) *A zoomed in contour plot of the temperature distribution at the top of the substrate near the heat source using back feeding*

Fig. 4.15 *A zoomed in contour plot of the temperature distribution near the heat source for front feeding (a), and for back feeding (b).*

Figure 4.16a shows the temperature distribution on the bottom of the substrate after 35 seconds of deposition. Figure 4.16b shows the temperature distribution after 215 seconds. In Figure 4.16b the global temperature has increased by approximately 76 % compared to Figure 4.16a.

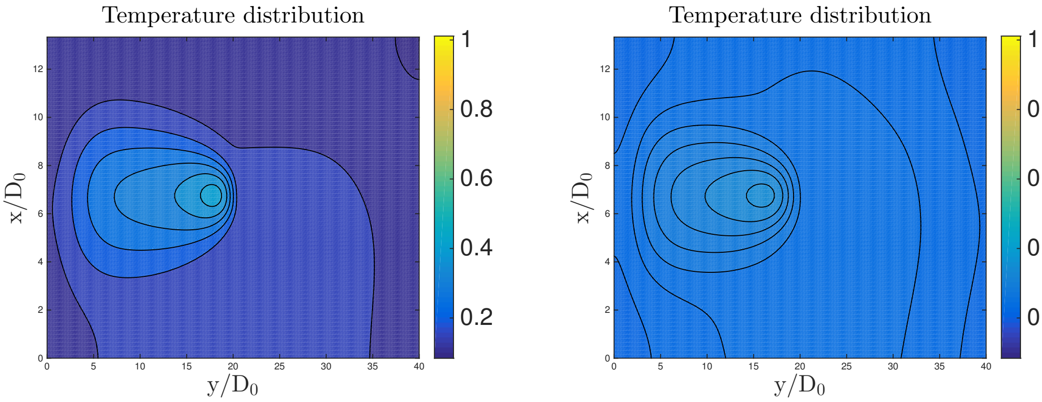

(a) *A contour plot of the temperature distributions at the bottom of the substrate after 35 seconds of deposition.*

(b) *A contour plot of the temperature distributions at the bottom of the substrate after 215 seconds of deposition.*

Fig. 4.16 *Contour plots of the temperature distribution at the bottom of the substrate after 35 seconds (a), and after 215 seconds (b) of deposition.*

4.4.2 Melt depth & maximum temperature

This section presents the results of the melt depth D and maximum temperature T_{max} when varying the laser power, traverse speed and wire feed rate to 80 % and 120 % of the nominal values, and the pause times with 50 % and 75 % of the nominal value.

4.4.2.1 Different pause times

Figure 4.17a illustrates the melt depth versus deposition time for different values of pause times between the deposition of strings. Vertical lines represent the deposited layer height. A pause time half of the nominal value results in a melt depth corresponding to three layers after 175 seconds of deposition. This means that the pause time needs to be decreased in order to achieve a melt depth that reaches the substrate when the third layer is under deposition. Figure 4.17b illustrates the maximum temperatures for different pause times. Vertical lines represents the critical temperatures, Tk_0, Tk_1, Tk_2, Tk_3. Logically, the results indicate that shorter pause times result in overall higher temperatures, thus larger melt depths. Also, since the microstructure is dependent on the time the temperature is below Tk_0 before is rises, the paus times alter the microstructure.

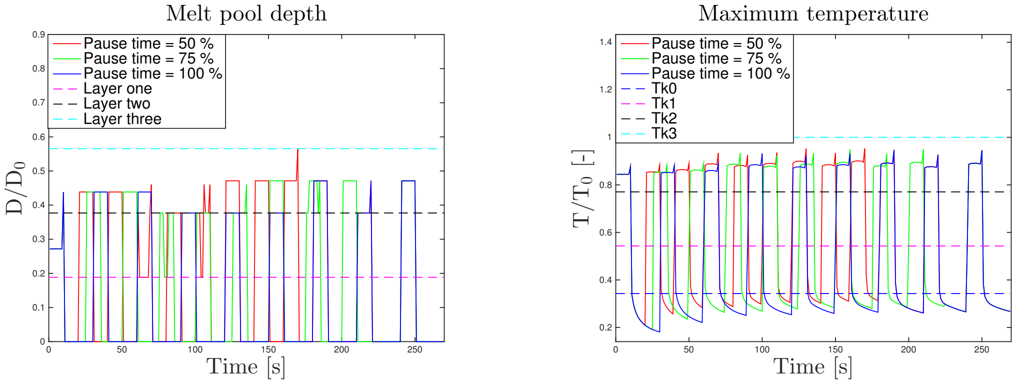

(a) *The melt depth versus time for different pause times.*

(b) *The maximum temperature versus time for different pause times.*

Fig. 4.17 *The melt depth (a), and maximum temperature (b) versus time for different pause times.*

4.4.2.2 Different laser powers

Figure 4.18a and Figure 4.18b illustrate the melting depth, and maximum temperatures for different values of the laser power. The melting depth is directly related to the maximum temperature, which depends on the incident power. The melt depth penetrates down to a depth corresponding to approximately three layer heights when using a laser power of 120 % of the nominal value, as can be observed in Figure 4.18a. A laser power of 120 % also results in the upper critical temperature limit Tk_3 being reached after only 100 seconds of deposition, see Figure 4.18b.

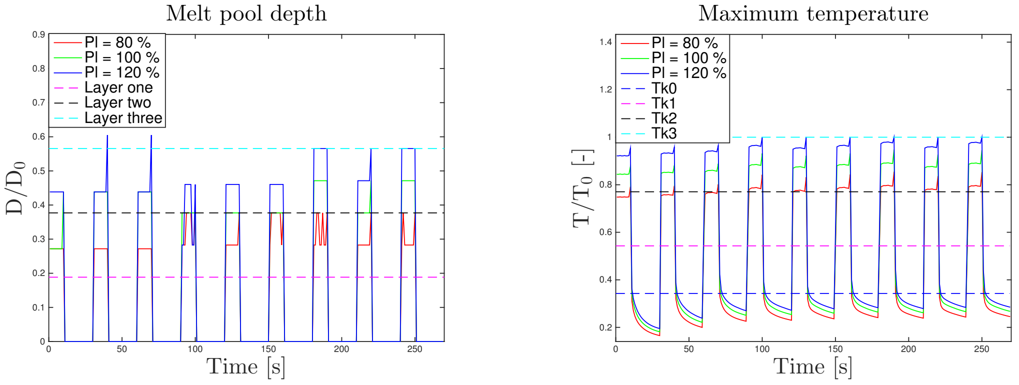

(a) *The melt depth versus time for different laser powers.*

(b) *The maximum temperature versus time for different laser powers.*

Fig. 4.18 *The melt depth (a), and maximum temperature (b) versus time for different laser powers.*

4.4.2.3 Different traverse speeds and wire feed rates

Figure 4.19b and Figure 4.19a show the melting depth, and maximum temperatures for different values of the traverse speed and wire feed rate. Low traverse speeds and wire feed rates increases the energy input per unit length. This results in higher maximum temperatures, and deeper melting depths. Conversely, higher traverse speeds and wire feed rates results in lower energy input per unit length.

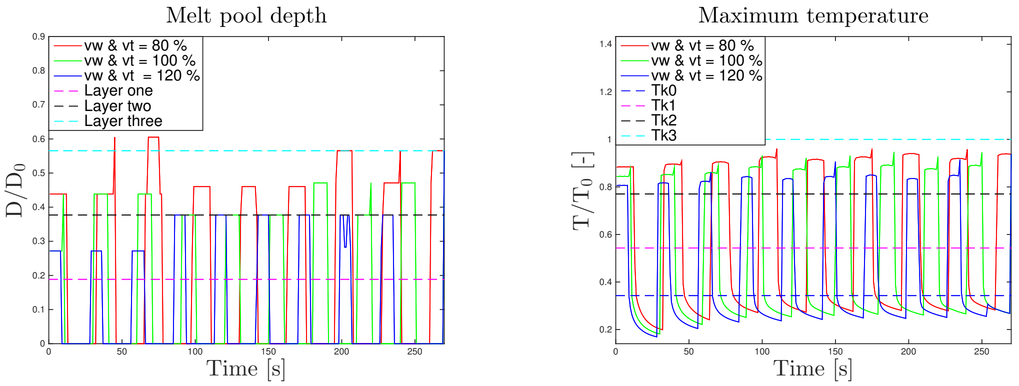

(a) *The maximum temperature versus time for different wire feed rates and traverse speeds.*

(b) *The melt depth versus time for different wire feed rates and traverse speeds.*

Fig. 4.19 *The melt depth (a), and maximum temperature (b) versus time for different wire feed rates and traverse speeds.*

4.5 Process control

By controlling the process parameters described in section 2.1.1, a stable deposition can be ensured, where the deposition process is smooth and kept within reasonable temperature limits. In this thesis work, the main focus has been on the three main process parameters (traverse speed, wire feed rate and laser power). Figure 4.20 shows the process window established by studying T_{max} for different values of the laser power and the traverse speed/wire feed rate, under fixed layer height, front-feeding and an initial substrate temperature set to 100 % of the nominal value. The vertical axis P/P_0, represents the normalised laser power, and the horizontal axis, v_t/v_0 the normalised traverse speed, and v_w/w_0 the normalised wire feed rate. The right filled area illustrates the values of the process parameters that can be applied without T_{max} exceeding the boiling temperature of aluminium, T_{bAl}, and at the same time, stay above the melting temperature of Ti64, T_{m2}. The left filled area illustrates the set of values of the process parameters that can be applied so that T_{max} is above the boiling point of aluminium, but under the boiling temperature of titanium, T_{bTi}.

Approaching too near T_{m2} will result in incomplete melting, and no fusion bond will form between the deposited wire and substrate. On the opposite, a temperature above the boiling temperature of aluminium, and eventually the boiling temperature of titanium, causes the material to evaporate, changing the composition and thereby damaging the material components and creating pores. To achieve a constant layer height when changing the traverse speed, the wire feed rate will have to be equally changed. Thus, for constant layer height, the process windows for the traverse speed and wire feed rates, are equally shaped.

Using back feeding increases T_{max} by approximately 80 K, which allows for higher traverse speeds and feed rates compare to front feeding, thus resulting in a small offset of the process window to the right in Figure 4.20.

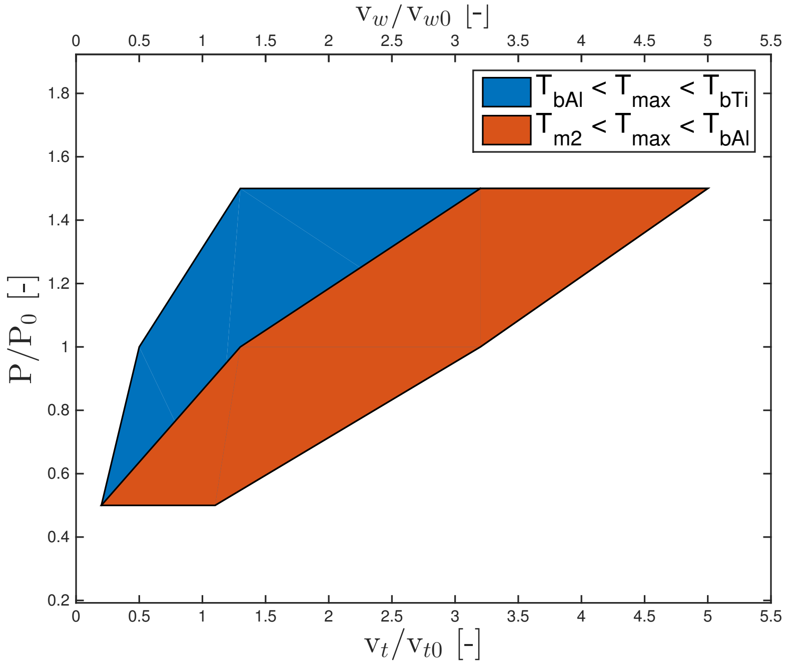

Fig. 4.20 *A process window established by studying T_{max} for the laser power, traverse speed and wire feed rate. The limits are the boiling temperature of Ti64, the boiling temperature of aluminium, and the boiling temperature of Ti64.*

Establishing a process window for smooth deposition, the temperature of the newly deposited node T_{dn} rather than T_{max} should be studied. T_{dn} can be found by using Eq (3.2). Figure 4.21 shows the viable traverse speeds and wire feed rates in relation to power input if T_{nd} is to be kept within interval $T_{m2} < T_{dn} < T_{m2} + 100\ K$. A temperature of the deposited wire larger than the melting temperature will result in globular transfer, and a temperature lower than the melting temperature will result in plunging. Compared to Figure 4.20, the window is substantially more narrow, and indicates whether the deposition is smooth, globular or plunging.

Higher laser power slightly widens the process window, opening the possibility for higher deposition rates. This is because the traverse speed governs the energy input per length, and with higher feed rates, the more energy can be absorbed. For lower traverse speeds and wire feed rates, more energy goes directly into the substrate which causes the temperature limits to be exceeded. Too high rates causes LOF, as the energy input is not sufficiently large.

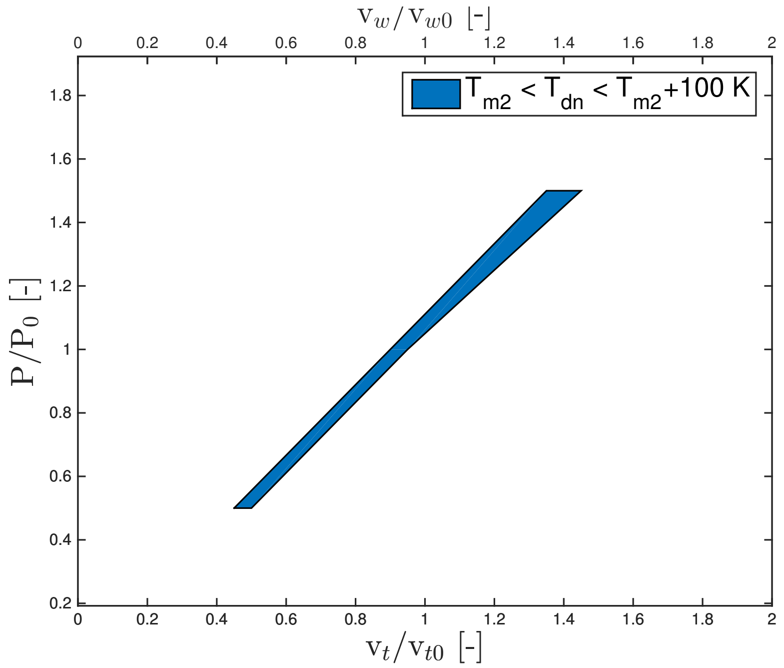

Fig. 4.21 *A process window established by studying T_{dn} for the laser power, traverse speed and wire feed rate. The limits are the melting temperature of Ti64 and the melting temperature of Ti64 + 100 K.*

5

Discussion

As the main part of the analysis and discussion was covered in the result section, a more thoroughly reflection that covers model-accuracy and future work is presented here.

5.1 Accuracy

The accuracy of the created LMwD simulation program is relatively high for one layer deposition, but less accurate when simulating several layers of deposition (compare Figure 4.1-4.2). This could be due to the differences in heights of the layers in the simulations and the heights of the layers in the process trials, an error which increases with additional layers. It could also be an indicator of possible errors in the algorithm, or simply a result of the assumptions described in Section 3.5.1.

A grid size of 1 mm was used for the substrate during the 700 seconds simulations presented in Section 4.1, and it is left to investigate how the results are affected when using smaller substrate grid spacing for several layers of deposition. Also, the result presented in Section 4.2.2 is not satisfying as it shows that the solution is still grid dependent. Thus, a sensitivity analysis of grid spacings less than 0.3 mm is left to be conducted. An explanation for the relatively large differences of the curves seen in the sensitivity analysis of the grid spacing, Figure 4.4, could be that the locations of the thermocouples is not same for 0.3 mm, 1 mm and 0.5 mm grid spacings, since 0.3 is not divisible with 1.0 or 0.5, and a slight offset of the thermocouple could result in high temperature differences, as seen in Figure 4.10-4.11. The unrealistic heat transfer coefficient described in Section 4.3.1 could be a result of the grid dependence, or simply an error in the linearization and implementation of the radiation boundary condition.

The largest differences in Figures 4.1-4.2 of approximately 30 % is a result of phase offsets, which most likely is a result of thermocouple displacement, or errors in the implemented thermodynamic properties of Ti-6Al-4V, which affects the "temperature momentum", causing the temperature to rise too early or too late when the heat source is moving past the concerning area. Since the thermocouples were placed on the substrate surface, further comparisons with simulations and experimental data are needed to evaluate the temperature accuracy within the substrate and the deposited layers. In comparison with conventional FEM simulations for temperature distributions, the program is fast. However, to be able to simulate larger structures for longer periods of deposition, the program needs to be less computational demanding.

5.2 Future Work

The main focus of the future work should lie in the process of making the model less computational demanding, and thereby lowering the simulation time needed to produce accurate results for large scale deposits. This could be done by making the mesh adaptive, e.g. applying high resolution in areas only near and inside the melt pool. Alternatively, applying linear temperature functions for low gradient areas, see Figure 4.12b, would further lower the amount of calculations needed. It is also of uttermost importance that smaller grid spacings are tested to further evaluate the grid dependence and its affect on cooling. Also, a different implementation of the boundary conditions should be tested. As described earlier, investigating different temperature distributions and geometrical shapes purely by traditional manufacturing trials would be very expensive. Instead, simulations could serve as a cost effective method to explore thermal history under different process setups. Further work will include setting up simulations describing upcoming process trials, trials that will involve more complex and larger structures.

6

Conclusion

The created simulation model for LMwD shows promising potential in producing accurate and fast temperature approximations. The simulation values coincide with the experimental values in a satisfactory manner, and the maximum deviations of approximately 30 % is due to phase offsets, which most likely is a result of thermocouple displacement or errors in the implemented thermodynamic properties of Ti-6Al-4V. The intensity of the incident laser power was found to have a large impact on local temperature and melt depth as it is directly related to the maximum temperature. Initial wire temperature and ambient temperatures were found to have a negligible impact on the temperature accuracy.

Higher laser powers allow for higher deposition rates as the process window inclines towards higher feed rates and traverse speeds. Thus, a high laser power can melt larger quantities of material at a faster pace, but also requires higher traverse speed as the energy input per unit length increases. Low laser powers require low feed rates in order to avoid too low melt depths, or in worst case, incomplete melting.

Bibliography

[1] Kinsella M E. and Carlson D. Additive manufacturing overview: The qualification pathway. 2015.

[2] Heralić A. Månsson T., Forsman S. and Sjunnesson A. Proposed qualification strategy for additively manufactured materials in load carrying applications for jet engines.

[3] Skystedt F. Pederson R., Berglund D. and Warren R. Modelling and experimental calibration of electron beam welded ti-6al-4v.

[4] Heralić A. *Monitoring and Control of Robotized Laser Metal-Wire Deposition.* PhD thesis, Chalmers University of Technology, 2012.

[5] Lundbäck A. and Lindgren L E. Finite element in analysis and design. 2011.

[6] Yunus A. *Introductions to Thermodynamics and Heat Transfer.* The McGraw-Hill Companies, Inc., Boston, Massachusetts, 1997.

[7] Wilson E R. Welty R J., Wicks E C. and Rorrer L G. *Fundamentals of Momentum, Heat, and Mass Transfer.* John Wiley & Sons, Inc., River Street, Hoboken, 2008.

[8] Welsch G. Boyer R. and Codings E W. *Materials Properties Handbook: Titanium Alloys.* ASM International, Materials Park, OH, 2007.

[9] Babu B. and Lindgren L E. Dislocation density based model for plastic deformation and globularization of ti-6al-4v. 2013.

[10] Eyraud V. Nadal M H. Wilthan B. Cagran C., Doytier D. and Pottlacher G. Thermophysical properties of solid and liquid ti-6al-4v (ta6v) alloy. 2006.

[11] ASM Aerospace Specification Metals Inc. Titanium ti-6al-4v-ams-4911, 2016.

[12] Taylor R. Cezairliyan A., McClure J L. Thermophysical measurements on 90ti-6ai-4v alloy above 1450 k using a transient (subsecond) technique*. 1977.

[13] Davim J P. Veiga C. and Loureiro A J R. Properties and applications of titanium alloys. 2012.

[14] Lubadovic M. and Kovacevic R. Modelling of the laser surface nitriding of ti-6al-4v alloy - analysis of heat transfer and residual stresses. 2001.

[15] Ferziger J H. and Perić M. *Computational Methods for Fluid Dynamics.* Springer-Verlag, Heidelberg, New York, 2002.

[16] Versteeg H K. and Malalasekera W. *An Introduction to Computational Fluid Dynamics.* Pearson Education Limited, Edinburgh Gate, 2007.

[17] Pentenrieder B. Finite element solutions of heat conduction problems in complicated 3d geometries using the multigrid method. Master's thesis, Technische Universitat at Munchen, 2005.